AD-A022 649

DEVELOPMENT OF A PROJECTILE PENETRATION THEORY.
REPORT 2. DEEP PENETRATION THEORY FOR HOMOGENEOUS
AND LAYERED TARGETS

Robert S. Bernard

Army Engineer Waterways Experiment Station
Vicksburg, Mississippi

February 1976

REPORT DOCUMENTATION PAGE		READ INSTRUCTIONS BEFORE COMPLETING FORM
1. REPORT NUMBER Technical Report S-75-9	2. GOVT ACCESSION NO.	3. RECIPIENT'S CATALOG NUMBER
4. TITLE (and Subtitle) DEVELOPMENT OF A PROJECTILE PENETRATION THEORY; Report 2, Deep Penetration Theory for Homogeneous and Layered Targets		5. TYPE OF REPORT & PERIOD COVERED Report 2 of a Series
		6. PERFORMING ORG. REPORT NUMBER
7. AUTHOR(s) Robert S. Bernard		8. CONTRACT OR GRANT NUMBER(s)
9. PERFORMING ORGANIZATION NAME AND ADDRESS U. S. Army Engineer Waterways Experiment Station Soils and Pavements Laboratory P. O. Box 631, Vicksburg, Miss. 39180		10. PROGRAM ELEMENT, PROJECT, TASK AREA & WORK UNIT NUMBERS Project 4A161102B52E, Task 04, Work Unit 13
11. CONTROLLING OFFICE NAME AND ADDRESS Office, Chief of Engineers, U. S. Army Washington, D. C. 20314		12. REPORT DATE February 1976
		13. NUMBER OF PAGES 70
14. MONITORING AGENCY NAME & ADDRESS(if different from Controlling Office)		15. SECURITY CLASS. (of this report) Unclassified
		15a. DECLASSIFICATION/DOWNGRADING SCHEDULE

16. DISTRIBUTION STATEMENT (of this Report)

Approved for public release; distribution unlimited.

17. DISTRIBUTION STATEMENT (of the abstract entered in Block 20, if different from Report)

18. SUPPLEMENTARY NOTES

19. KEY WORDS (Continue on reverse side if necessary and identify by block number)

Projectile penetration

20. ABSTRACT (Continue on reverse side if necessary and identify by block number)

Existing shallow penetration theory (which is based on cavity expansion theory) is modified and extended for application to deep penetration in homogeneous and layered targets. This is accomplished by means of a postulated relation between the target penetration resistance and the so-called "solid Reynolds number." The predictions of the modified theory are shown to be

(Continued)

DD FORM 1473 EDITION OF 1 NOV 65 IS OBSOLETE

20. ABSTRACT (Continued)

in approximate agreement with experimental, empirical, and two-dimensional finite-difference results for shallow as well as deep penetration in metal, rock, concrete, and cohesive soil targets.

PREFACE

The investigation reported herein was conducted by personnel of the Soil Dynamics Division (SDD), Soils and Pavements Laboratory (S&PL), U. S. Army Engineer Waterways Experiment Station (WES), as a part of DA Project No. 4A16110?B52E, "Fragment and Projectile Penetration Resistance of Soils," Task 04, Work Unit 13.

The theoretical developments were originated by Mr. R. S. Bernard during the period July 1974 to January 1975 under the supervision of Dr. J. G. Jackson, Jr., Chief, SDD. Messrs. J. P. Sale and R. G. Ahlvin were Chief and Assistant Chief, S&PL, respectively. SP5 D. C. Creighton developed and executed the necessary computer codes, and Drs. B. Rohani and P. F. Hadala provided continuous technical and moral support. This report was prepared by Mr. Bernard.

COL G. H. Hilt, CE, was Director of WES during the investigation and at the time of publication of this report. Mr. F. R. Brown was Technical Director.

CONTENTS

2

CONVERSION FACTORS, U. S. CUSTOMARY TO METRIC (SI) UNITS OF MEASUREMENT

U. S. customary units of measurement used in this report can be converted to metric (SI) units as follows:

Multiply	By	To Obtain
inches	2.54	centimetres
feet	0.3048	metres
square inches	6.4516	square centimetres
pounds (mass)	0.4535924	kilograms
pounds (mass) per cubic foot	16.01846	kilograms per cubic metre
pounds (force) per square inch	6894.757	pascals
feet per second	0.3048	metres per second

Note: 1 kilobar = 1,000 bars = 14,500 pounds per square inch = 100 megapascals.

DEVELOPMENT OF A PROJECTILE PENETRATION THEORY

DEEP PENETRATION THEORY FOR HOMOGENEOUS AND LAYERED TARGETS

PART I: INTRODUCTION

Background

1. Projectile penetration has been the object of theoretical and experimental investigations for at least two centuries. However, until recent years, reliable penetration predictions were achieved only by means of empirical equations using various target resistance functions and pseudoconstants which were drawn directly from penetration experiments. The first successful analysis on purely theoretical grounds was apparently due to Bishop, Hill, and Mott,[1] who related quasi-static punch indentation to the static expansion of spherical and cylindrical cavities in an infinite medium. In a later development which incorporated an ad hoc analogy with the dynamic expansion of a spherical cavity in an infinite medium,[2] Goodier[3] formulated a dynamic penetration theory for rigid spherical projectiles which is applicable to elastic-plastic strain-hardening targets. In subsequent efforts, attempts were made to account for the effects of target compressibility[4] and projectile nose shape,[5] but the substance of the Goodier penetration theory remained unchanged.

2. A useful penetration theory must be fairly simple in order that reliable predictions can be made with a minimal expenditure of time and money. A number of simplifying assumptions must be made in the development of such a theory; and since the objective is simply to obtain an equation of motion for the projectile, only the gross features of the target response may be taken into account. An extreme alternative to the simple theoretical approach is provided by two-dimensional (2D) finite-difference analyses which generally require large expenditures in man-hours and computer time. Nevertheless, a 2D finite-difference solution has the advantage that the details of projectile and target

behavior can be closely examined; and while an approach of this kind may be too costly and cumbersome for large-scale parameter studies, it can be extremely valuable for assessing the relative effects of various mechanisms in the penetration process.

3. At the present time, there is widespread need for a tractable theory which can be used to study the penetration of soil, rock, concrete, and metal targets by projectiles such as bombs, bullets, shell fragments, and missiles. Such a theory is needed from both the offensive and defensive viewpoints since a theory which analyzes the penetration process can also be used to determine the conditions under which final penetration depth is maximized or minimized, respectively. In July 1973, a small research effort was initiated under the sponsorship of the Office, Chief of Engineers (OCE), to develop a penetration theory which would account for the penetration of homogeneous and layered targets by rigid axisymmetric projectiles. In the period July 1973 to June 1974, the previously existing Goodier theory for spherical projectiles[3,4] was extended for projectiles with conical and ogival nose shapes at shallow to moderate depths, as reported in Reference 5. In the present report this theory is modified and extended to account for deep penetration of homogeneous and layered targets at very high impact velocities. However, it is emphasized that the modified theory is still applicable to shallow penetration problems and produces approximately the same results as the unmodified theory at low impact velocities. The theory developed herein supersedes all preceding work and is applicable for shallow and deep penetration in cohesive targets. The developments presented in this report are the results of efforts conducted under the OCE program during the period July 1974 to January 1975.

Purpose

4. The purpose of this investigation is to build upon existing penetration theory[5] to develop a more general theory for cohesive targets which is valid for deep penetration at very high impact velocities as well as for shallow penetration at low impact velocities. As in

previous work, the fundamental basis for the penetration theory is the dynamic cavity expansion theory,[3-5] and the modification for high-speed, deep penetration is accomplished through a postulated relation between target penetration resistance and the "solid Reynolds number," which was first introduced in Reference 5.

Scope

5. This report is intended to be a self-contained document on the subject of projectile penetration theory for cohesive targets, and it is structured such that each part may be read independently or in sequence, depending on the interests of the reader. The cavity expansion theory is discussed in Part II. Previous work in shallow penetration theory is outlined in Part III, followed by the modifications whereby the theory is extended for deep penetration. Practical applications of the theory are presented in Part IV, and conclusions and recommendations are stated in Part V.

Background

6. The dynamic expansion of spherical cavities in solids has been investigated by several authors.[2-5] Goodier[3] used the theory of dynamic cavity expansion in an incompressible strain-hardening material[2] as the basis of a penetration theory for rigid spherical projectiles and homogeneous targets. In Reference 5, the cavity expansion theory was extended to concentrically layered compressible media and was used as the basis of a projectile penetration theory for layered targets. The cavity expansion theory developed in Reference 5 represents a first attempt at a theory for concentrically layered media and is more complicated than necessary. In the following discussion, a simplified version of the cavity expansion theory for concentrically layered media will be presented and will provide a smoother transition to the penetration theory than does the more complicated version.

Problem Formulation

7. Consider a spherical cavity of radius a(t) surrounded by two concentric layers of different materials, as shown in Figure 1. These materials exhibit elastic-plastic response with linear strain-hardening under shear stress, as illustrated in Figure 2. Both

Figure 1. Spherical cavity expansion in a concentrically layered medium
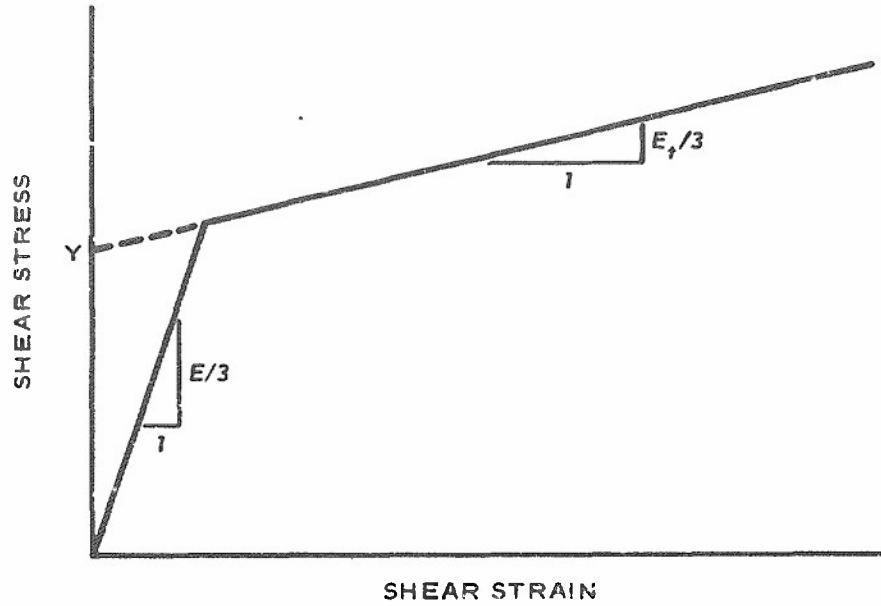
7
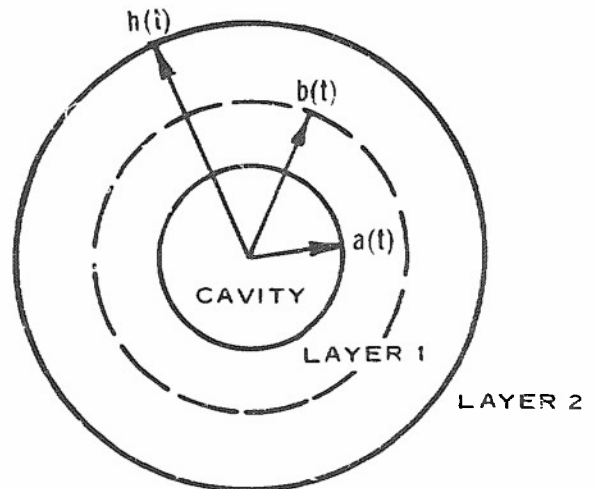
Figure 2. Material behavior in shear

materials exhibit ideal locking compressibility[4] under hydrostatic
stress such that transition from the elastic to plastic states is ac-
companied by a small but finite volumetric strain known as the locking
strain

$$\epsilon_\ell = \ln \frac{\rho_0}{\rho_\ell} \tag{1}$$

where ρ_0 and ρ_ℓ are the material densities in the elastic and locked
plastic states, respectively, and $|\epsilon_\ell| \ll 1$. Otherwise, the materials
are incompressible, and the regions of elastic and locked plastic be-
havior are separated by a weak plastic shock front of radius $b(t)$,
where t denotes time. Accordingly, the locking condition on strain is

$$\epsilon_r + 2\epsilon_\theta = \begin{cases} \epsilon_\ell , & a < r < b \\ 0 , & r > b \end{cases} \tag{2}$$

where $\epsilon_r(r, t)$ and $\epsilon_\theta(r, t)$ are normal strains in the radial and cir-
cumferential directions, respectively, with r as the radial coordinate.
The associated strain rates are related to the outward radial particle
velocity $v(r, t)$ by

8

$$\overset{\circ}{\varepsilon}_r = \frac{\partial v}{\partial r} \; ; \quad \overset{\circ}{\varepsilon}_\Theta = \frac{v}{r} \tag{3}$$

where a dot above any quantity denotes a time derivative. Equations 2 and 3 give rise to

$$v(r, t) = \begin{cases} \dfrac{f_\ell(t)}{r^2} \; , & a < r < b \\[4mm] \dfrac{f_e(t)}{r^2} \; , & r > b \end{cases} \tag{4}$$

where $f_\ell(t)$ and $f_e(t)$ are unknown functions. The stress-strain relation for the material in shear is[4]

$$\sigma_\Theta - \sigma_r = \begin{cases} Y + 2E_t(\varepsilon_\Theta - \dfrac{1}{3}\varepsilon_\ell) \; , & a < r < b \\[4mm] 2E\varepsilon_\Theta \; , & r > b \end{cases} \tag{5}$$

where $\sigma_r(r, t)$ and $\sigma_\Theta(r, t)$ are normal stresses in the radial and circumferential directions and Y , E , and E_t are the yield strength, elastic modulus, and strain-hardening modulus, respectively, for the material in compression. The geometry is spherically symmetric, and the material equation of motion is

$$\frac{\partial \sigma_r}{\partial r} + \frac{2}{r}(\sigma_r - \sigma_\Theta) = \rho\left(\frac{\partial v}{\partial t} + v\frac{\partial v}{\partial r}\right) \tag{6}$$

where ρ is the local density. After combining Equations 4, 5, and 6, the resulting equation is integrated from $r = \infty$ to $r = a(t)$, subject to the condition that the material is stress-free as $r \to \infty$. The equation for the compressive normal stress $p = -\sigma_r[a(t)]$ at the cavity surface is then found to be:

9

$$p = \Delta\sigma_b + \int_a^b \rho_\ell \left(\frac{\dot{f}_\ell}{r^2} - \frac{2f_\ell^2}{r^5} \right) dr$$

$$+ \int_b^\infty \rho_0 \left(\frac{\dot{f}_e}{r^2} - \frac{2f_e^2}{r^5} \right) dr$$

$$+ 2 \int_a^b \left\{ Y + 2E_t \left[\epsilon_\theta(r, t) - \frac{1}{3} \epsilon_\ell \right] \right\} \frac{dr}{r} + 4 \int_b^\infty E\epsilon_\theta(r, t) \frac{dr}{r} \quad (7)$$

where $\Delta\sigma_b$ is the discontinuity in σ_r at $r = b(t)$, given by

$$\Delta\sigma_b = \sigma_b^{(+)} - \sigma_b^{(-)} \quad (8)$$

and $\sigma_b^{(+)}$ and $\sigma_b^{(-)}$ are the limiting values of σ_r as $r \rightarrow b$ in the elastic and locked plastic regions, respectively.

Problem Solution

8. In order to evaluate Equation 7 and thereby obtain an explicit relation between p and $a(t)$, relations must be established between $a(t)$ and $f_\ell(t)$, $f_e(t)$, $\Delta\sigma_b(t)$, $h(t)$, $b(t)$, and $\epsilon_\theta(r, t)$. The first of Equations 4 is evaluated at $r = a$ leading to

$$f_\ell = a^2 \dot{a} \quad (9)$$

The jump condition for conservation of mass is applied at $r = b$ so that

$$\rho_\ell [\dot{b} - v^{(-)}] = \rho_0 [\dot{b} - v^{(+)}] \quad (10)$$

where $v^{(+)}$ and $v^{(-)}$ are the limiting values of v as $r \rightarrow b$ in the elastic and locked plastic regions, respectively. After evaluating

10

Equation 4 at $r = b$ and combining the results with Equations 9 and 10, the following is obtained:

$$f_\theta = \frac{a^2\dot{a} - \alpha b^2 \dot{b}}{1 - \alpha} \qquad (11)$$

where α is the material compaction coefficient defined by

$$\alpha = 1 - \frac{\rho_0}{\rho_\ell} \cong -\epsilon_\ell \qquad (12)$$

which is limited to $\alpha \ll 1$ since attention has been restricted to $|\epsilon_\ell| \ll 1$. The jump condition for conservation of momentum is applied at $r = b$ so that

$$\Delta\sigma_b = \rho_\ell v^{(-)}\left[\dot{b} - v^{(-)}\right] - \rho_0 v^{(+)}\left[\dot{b} - v^{(+)}\right] \qquad (13)$$

Evaluating Equation 4 at $r = b$ and then combining the results with Equations 9, 11, 12, and 13 leads to

$$\Delta\sigma_b = \frac{\alpha\rho_\ell \dot{b}^2(1 - a^2/b^2)^2}{1 - \alpha} \qquad (14)$$

For large deformations, the circumferential strain can be appropriately expressed as

$$\epsilon_\theta = \ln \frac{r}{r_o} \qquad (15)$$

where r_o is the initial position of a particle located at position r. Restricting attention to situations where $Y \ll E$, $E_t \ll E$, and $|\epsilon_\ell| \ll 3Y/2E_t$, then

$$\epsilon_\theta[b(t)] = \ln \frac{b}{b_o} \cong \beta \qquad (16)$$

subject to $\beta \ll 1$ where b_o is the initial position of a particle located at $r = b$, and

11

$$\beta = \frac{Y}{2(E - E_t)} \tag{17}$$

9. Attention is now restricted to materials which have identical values of α and ϵ_ℓ. (This restriction can be relaxed by establishing appropriate composite values of α and ϵ_ℓ for the two layers.) Approximations for $\epsilon_\theta(r, t)$, $b(t)$, and $h(t)$ will now be obtained subject to the following assumptions:

a. Prior to the arrival of the plastic front at the initial layer interface location (i.e., $b < h_o$), the entire second layer is in the elastic state, and the location of the interface is approximately $h(t) \cong h_o$.

b. After the plastic front arrives at the initial layer interface position (i.e., $b \geq h_o$), the locked plastic region extends into the second layer, and the motion of the interface is no longer neglible.

10. Considering first the situation when $b < h_o$ and $a^3(t) \gg a^3(0)$, conservation of mass in the locked plastic region[4] gives rise to

$$r^3 - a^3 \cong (1 - \alpha)r_o^3 \ , \ a < r < b \tag{18}$$

Rearranging Equation 18 and then combining the result with Equation 15 yields the expression

$$\epsilon_\theta(r, t) - \frac{1}{3}\epsilon_\ell \cong - \frac{1}{3} \ln\left(1 - \frac{a^3}{r^3}\right) \ , \ a < r < b \tag{19}$$

Conservation of mass in the elastic region of the first layer requires that

$$r^3 - b^3 = r_o^3 - b_o^3 \ , \ b < r < h_o \tag{20}$$

The approximate relation obtained from rearranging Equation 20 and consolidating the result with Equations 15 and 17 is

$$\epsilon_\theta(r, t) \cong \frac{\beta_1 b^3}{r^3} \ , \ b < r < h_o \tag{21}$$

12

where β is given by Equation 17, and the subscript "1" denotes first layer material properties. Prior to the arrival of the plastic front at the initial interface location, the entire second layer is in the elastic state, and the circumferential strain is approximated by

$$\epsilon_\theta(r, t) \cong \frac{\beta_2 h_o^3}{r^3} \quad , \quad b < h_o < r \tag{22}$$

which is analogous to Equation 21 for the first layer. The subscript "2" denotes second layer material properties. Although Equation 22 is only approximately correct, the error which is introduced in Equation 7 is the same order of magnitude as the error which results from the assumptions (a) that $h \cong h_o$ when $b < h_o$ and (b) that the entire second layer is in the elastic state when $b < h_o$. Then the substitution of b and b_o for r and r_o, respectively, in Equation 18 results in

$$b^3 \cong \frac{a^3}{\delta_1} \quad , \quad b < h_o \tag{23}$$

where

$$\delta_i = \alpha + 3\beta_i \quad , \quad i = 1, 2 \tag{24}$$

and the subscripts "1" and "2" again denote first and second layer material properties. Note that the criterion $b < h_o$ is now equivalent to $a < \delta_1^{1/3} h_o$.

11. Now considering the situation when $b \geq h_o$ $\left(\text{i.e., when } a \leq \delta_1^{1/3} h_o \right)$, Equations 18 and 19 are applicable to the locked plastic regions in both layers. Furthermore, the motion of the interface is no longer neglible, and

$$h^2 \dot{h} = a^2 \dot{a} \quad , \quad b \geq h_o \tag{25}$$

Integrating Equation 25 from t_o to t yields

$$h^3 \cong a^3 + (1 - \delta_1) h_o^3 \quad , \quad b \geq h_o \tag{26}$$

where the initial conditions are $h(t_o) = h_o$ and $a(t_o) = \delta_1^{1/3} h_o$.
The circumferential strain in the elastic region is obtained by replacing β_1 with β_2 in Equation 21 so that

$$\varepsilon_\Theta(r, t) \cong \frac{\beta_2 b^3}{r^3} , \quad r > b \geq h_o \tag{27}$$

When $a^3 \gg \delta_1 h_o^3$, the relation between a and b must approach $b^3 \cong a^3/\delta_2$, which is analogous to Equation 23. Thus, the corresponding rate equation relating $\dot{a}$ and $\dot{b}$ must approach

$$b^2 \dot{b} \cong \frac{a^2 \dot{a}}{\delta_2} \tag{28}$$

where δ_2 is given by Equation 24. In order to obtain an approximate but continuous expression for b , Equation 28 is integrated from t_o to t , resulting in

$$b^3 \cong \frac{a^3}{\delta_2} + \frac{\delta_2 - \delta_1}{\delta_2} h_o^3 , \quad b \geq h_o \tag{29}$$

where the initial conditions are $b(t_o) = h_o$ and $a(t_o) = \delta_1^{1/3} h_o$.

Normal Stress at the Cavity Surface

12. Approximations have now been established relating $\varepsilon_\Theta(r, t)$, $b(t)$, $h(t)$, and $a(t)$ for the two cases $b < h_o$ and $b \geq h_o$ (i.e., $a < \delta_1^{1/3} h_o$ and $a \geq \delta_1^{1/3} h_o$, respectively). For the first case, Equations 9, 11, 14, 19, 21, 22, and 23 are used with $h \cong h_o$ to evaluate Equation 7. For the second case, Equations 9, 11, 14, 19, 26, 27, and 29 are used to evaluate Equation 7. In each case, the resulting expression for the compressive normal stress at the cavity surface has the form

$$p = p_s + p_I \tag{30}$$

where p_s is the contribution due to material shear, and p_I is the

14

contribution due to material inertia (i.e., the dynamic pressure at the cavity surface)

$$p_I = \rho_{\ell 1}\left(B_1 a\ddot{a} + B_2 \dot{a}^2\right) \tag{31}$$

where a, $\dot{a}$, and $\ddot{a}$ are the radial position, velocity, and acceleration of the cavity wall. With the exception of the inertial coefficients B_1 and B_2, the subscripts "1" and "2" are used to denote first and second layer properties, respectively. Prior to the arrival of the plastic front at the initial layer interface location, the expressions for p_s, B_1, and B_2 are

$$p_s(b < h_o) = -\frac{2}{3} Y_1 \ln \delta_1 + \frac{4}{9} E_{t1}\left(\frac{\pi^2}{6} - \sum_{m=1}^{\alpha} \frac{\delta_1^m}{m^2}\right)$$
$$+ \frac{4}{3}\beta_1 E_1\left(1 - \frac{a^3}{\delta_1 h_o^3}\right) + \frac{4}{3}\beta_2 E_2\left(\frac{a^3}{\delta_1 h_o^3}\right) \tag{32}$$

$$B_1(b < h_o) = 1 - \delta_1^{1/3} + \left(1 - \frac{\alpha}{\delta_1}\right)\left[\delta_1^{1/3} - \left(1 - \frac{\rho_{02}}{\rho_{01}}\right)\frac{a}{h_o}\right] \tag{33}$$

$$B_2(b < h_o) = 2B_1 + \frac{(1 - \delta_1)^2}{\delta_1^{2/3}(1 - \alpha)} - \frac{1}{2}\left(1 - \delta_1^{4/3}\right)$$

$$- \frac{\left(1 - \frac{\alpha}{\delta_1}\right)^2}{2(1 - \alpha)}\left[\delta_1^{4/3} - \left(1 - \frac{\rho_{02}}{\rho_{01}}\right)\frac{a^4}{h_o^4}\right] \tag{34}$$

After the arrival of the plastic front at the initial interface location, the expressions for p_s, B_1, and B_2 are

$$p_s(b \geq h_o) = 2Y_1 \ln \frac{h}{a} + \frac{4}{9} E_{t1} \left[\frac{\pi^2}{6} - \sum_{m=1}^{\infty} \frac{(a/h)^{3m}}{m^2} \right] + 2Y_2 \ln \frac{b}{h}$$

$$+ \frac{4}{9} E_{t2} \sum_{m=1}^{\infty} \left(\frac{1}{m^2}\right) \left[\left(\frac{a}{h}\right)^{3m} - \left(\frac{a}{b}\right)^{3m} \right] + \frac{4}{3} \beta_2 E_2 \qquad (35)$$

$$B_1(b \geq h_o) = 1 - \left(1 - \frac{\rho_{02}}{\rho_{C1}}\right) \frac{a}{h} - \frac{\alpha \rho_{02} a}{\delta_2 \rho_{01} b} \qquad (36)$$

$$B_2(b \geq h_o) = 2B_1 + \frac{\alpha \left(\frac{\rho_{02}}{\rho_{01}}\right)(1 - \delta_2)^2 \frac{a^4}{b^4}}{\delta_2^2(1 - \alpha)} - \frac{1}{2}\left[1 - \frac{a^4}{h^4} + \frac{\rho_{02}}{\rho_{01}}\left(\frac{a^4}{h^4} - \frac{a^4}{b^4}\right)\right]$$

$$- \frac{1}{2} \frac{\frac{\rho_{02}}{\rho_{01}}\left(1 - \frac{\alpha}{\delta_2}\right)^2 \frac{a^4}{b^4}}{1 - \alpha} \qquad (37)$$

where h and b are given, respectively, by Equations 26 and 29 for b > h$_o$.

13. When both layers have identical properties (i.e., when the medium is homogeneous), the layer subscripts are dropped, and Equations 31-37 reduce to

$$p_I = \rho_\ell \left(B_1 a\ddot{a} + B_2 \dot{a}^2 \right) \qquad (38)$$

$$p_s = -\frac{2}{3} Y \ln \delta + \frac{4}{9} E_t \left(\frac{\pi^2}{6} - \sum_{m=1}^{\infty} \frac{\delta^m}{m^2} \right) + \frac{4}{3} \beta E \qquad (39)$$

16

$$B_1 = 1 - \frac{\alpha}{\delta^{2/3}} \tag{40}$$

$$B_2 = \frac{3}{2} - \frac{\alpha}{\delta^{2/3}} \left[2 - \frac{(1 - \delta)^2}{1 - \alpha} \right] + \frac{1}{2} \delta^{4/3} \left[1 - \frac{(1 - \alpha/\delta)^2}{1 - \alpha} \right] \tag{41}$$

Material Compressibility

14. Throughout the development of the foregoing cavity expansion theory the compaction coefficient $\alpha \cong - \varepsilon_\ell \ll 1$ has been regarded as a material constant. This restriction is relaxed by allowing α to be a slowly varying function of pressure and then neglecting its derivatives. By taking this approach, it is possible to relate the appropriate instantaneous value of α to the dynamic pressure in the material adjacent to the cavity. Since the theory is already limited to small values of α, materials of interest are incompressible to a first approximation. For an incompressible homogeneous material, the volume-averaged dynamic pressure[5] in the plastic region $a < r < b$ is approximately

$$P_{ave} \cong \frac{3}{2} \rho_0 \left[a\ddot{a}\left(\delta_I^{1/3} - \delta_I + \delta_I^{4/3} \right) + \dot{a}^2 \left(2\delta_I^{1/3} - 3\delta_I + 3\delta_I^{4/3} \right) \right] \tag{42}$$

where

$$\delta_I = 3\beta \ll 1 \tag{43}$$

By using Equation 42 in conjunction with the pressure-density relation for a given material, a first approximation can be obtained for the compaction coefficient. When P_{ave} is sufficiently small, many materials can be characterized by the linear pressure-density relation

$$\alpha \cong \frac{P_{ave}}{\rho_0 C^2} \lll 1 \tag{44}$$

where C is the dilatational wave velocity in the material.

15. The cavity expansion theory for a concentrically layered

17

medium is restricted to materials with identical compaction coefficients.
However, this theory can be applied to materials with different compaction coefficients by estimating a composite compaction coefficient for both layers according to

$$\alpha = \alpha_1\left(1 - \frac{a}{h}\right) + \alpha_2\left(\frac{a}{h}\right) \tag{45}$$

where α_1 and α_2 are obtained from Equations 42 and 44 by using first and second layer properties, respectively. The effective locked plastic densities for the two layers are then

$$\rho_{\ell 1} = \frac{\rho_{01}}{1 - \alpha} \tag{46}$$

$$\rho_{\ell 2} = \frac{\rho_{02}}{1 - \alpha} \tag{47}$$

The particular expression for α which appears in Equation 45 is chosen so that the composite compaction coefficient will vary smoothly in a manner similar to the inertial coefficients B_1 and B_2.

PART III: PENETRATION THEORY

Background

16. The first successful theoretical investigation of the penetration process is apparently due to Bishop, Hill, and Mott,[1] who related quasi-static punch indentation to the static expansion of spherical and cylindrical cavities in an infinite medium. By means of an _ad hoc_ analogy with dynamic spherical cavity expansion,[2] Goodier[3] later developed a theory for the high-speed penetration of incompressible, strain-hardening targets by rigid spherical projectiles. Subsequently, Hanagud and Ross[4] modified the dynamic spherical cavity expansion theory in an effort to account for material compressibility and incorporated the results in Goodier's penetration theory. The next development came when Bernard and Hanagud[5] modified the Goodier theory in an attempt to account for the effect of projectile nose shape. Bernard and Hanagud also proposed a dimensionless parameter called the "solid Reynolds number" which serves as an order-of-magnitude index of the ratio of dynamic pressure to shear stress in the target and which can be used to some extent to determine the relative applicability of the theory in a particular penetration problem. Moreover, it was found that the range of applicability for the penetration theory in Reference 5 is restricted to low to moderate values of the solid Reynolds number (corresponding to shallow to moderate penetration depths). At high values of the solid Reynolds number (i.e., at very high velocities) the theory overpredicts the target resistance, resulting in an underprediction of final penetration depth. Accordingly, the Bernard-Hanagud version of the penetration theory will be referred to as the "shallow penetration theory," and the objective of the present investigation will be to develop a deep penetration theory which is applicable for very deep penetration as well as for shallow penetration in cohesive targets.

Shallow Penetration Theory

17. The basic assumptions in the shallow penetration theory are as follows:

a. The projectile is completely rigid.

b. The portion of the projectile frontal surface which is embedded in the target is in complete contact with the target.

c. Tangential stresses on the projectile frontal surface are negligible.

d. The compressive normal stress p on the frontal surface is given by

$$p = p_s + p_I \qquad (48)$$

where p_s is the contribution due to target behavior in shear and p_I is the dynamic pressure in the target adjacent to the frontal surface.

e. The shear contribution p_s is independent of projectile geometry, uniform over the frontal surface, and equal to the cavity expansion shear term, which is given by Equation 39 in Part II.

18. With these assumptions in mind, only the dynamic pressure term p_I remains to be determined in the expression for p. By drawing a loose analogy with the cavity expansion theory, Equation 38 is replaced with

$$P_I = \rho_\ell (B_1 a_o \ddot{q} + B_2 v_p^2) \qquad (49)$$

for fully embedded axisymmetric projectiles (Figures 3 and 4), where

ρ_ℓ = locked plastic density of the target

B_1, B_2 = inertial coefficients given by Equations 40 and 41

a_o = projectile radius

v_p = particle velocity in the target adjacent to the frontal surface

$\ddot{q}$ = projectile acceleration (the latter three terms replace a, $\dot{a}$, and $\ddot{a}$, respectively)

This then leaves the distribution of the particle velocity v_p to be specified along the frontal surface.
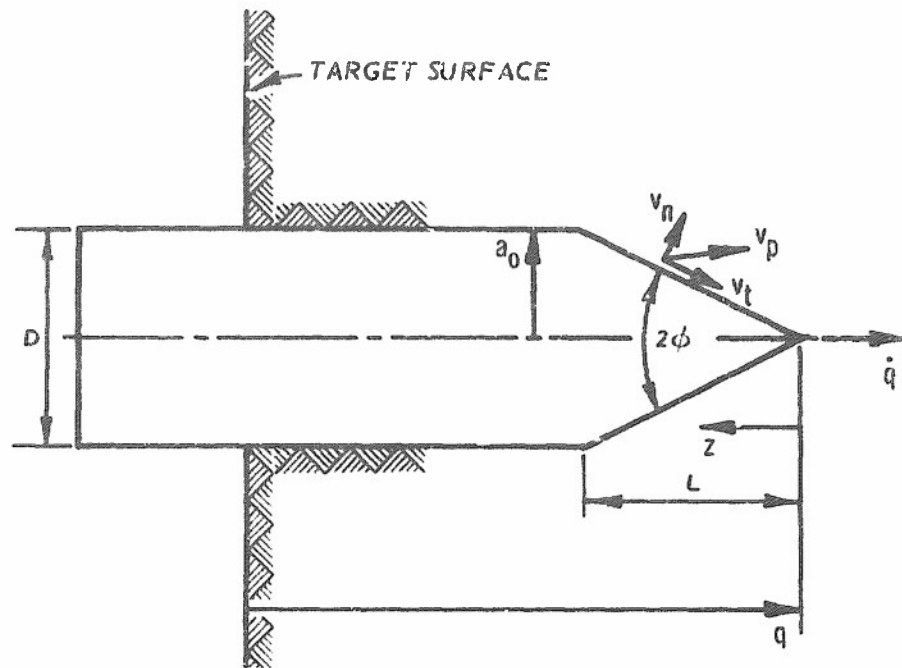
20

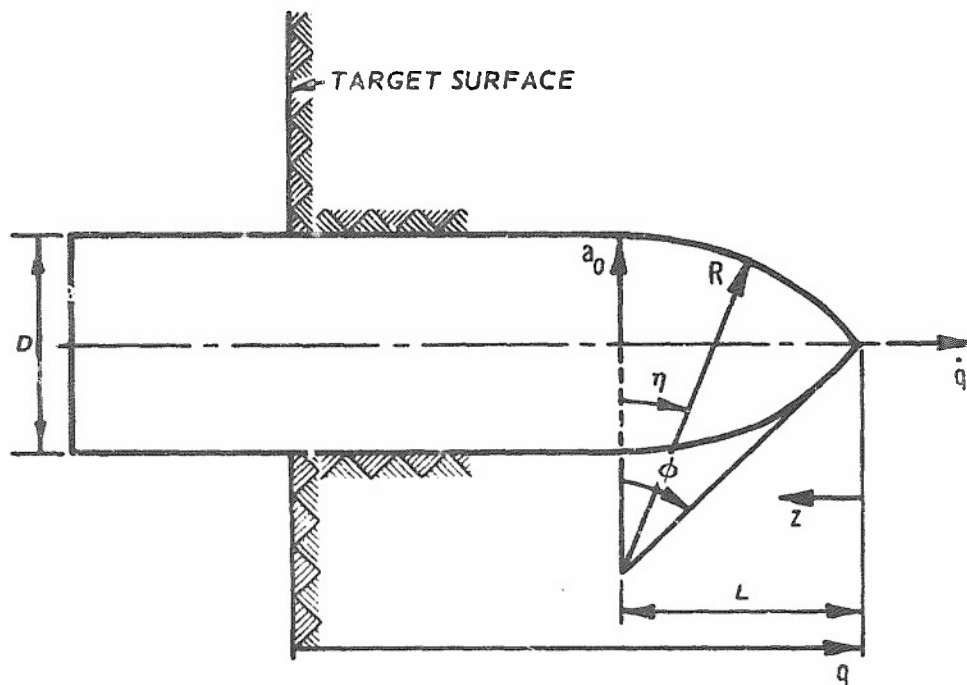Figure 3. Projectile with fully embedded
conical nose

Figure 4. Projectile with fully embedded
ogive nose

19. The constraints on particle motion along the frontal surface are as follows:

    <u>a</u>. The velocity of a particle at the nose tip $z = 0$ must be identical with the projectile velocity $\dot{q}$.

    <u>b</u>. Material cannot cross the projectile-target interface; thus the particle velocity component v_n, which is normal to the frontal surface, must be equal to the normal component of the projectile velocity.

    <u>c</u>. The particle velocity must be continuous on the frontal surface.

    <u>d</u>. Finally it is <u>assumed</u> that the particle velocity component v_t, which is tangent to the frontal surface, is zero at the base of the nose $z = L$, where z is axial distance from the nose tip and L is projectile nose length.

20. For the conical nose shown in Figure 3, v_n is given by

$$v_n = \dot{q} \sin \phi \tag{50}$$

where ϕ is the cone half-angle. The variation of v_t is <u>assumed</u> to be

$$v_t = (1 - x)^{1/2} \dot{q} \cos \phi \, , \, 0 \leq x \leq 1 \tag{51}$$

where the nondimensional cone position is denoted by

$$x = \frac{z}{L} \tag{52}$$

The resulting expression for v_p is then

$$v_p = \left(v_n^2 + v_t^2 \right)^{1/2} = \dot{q}(1 - x \cos^2 \phi)^{1/2} \tag{53}$$

For the ogive nose shown in Figure 4,

$$v_n = \dot{q} \sin \eta \tag{54}$$

and the equivalent dimensionless cone position is[5]

22

$$x_e(\eta) = \cos \eta \, \frac{\cos \eta - \cos \phi}{1 - \cos \phi \cos \eta} \tag{55}$$

where Equation 55 is analogous to Equation 52. Replacing x and ϕ with $x_e(\eta)$ and η, respectively, in Equation 51 leads to

$$v_t = [1 - x_e(\eta)]^{1/2} \, \dot{q} \cos \eta \;, \; 0 \leq \eta \leq \phi \tag{56}$$

so that

$$v_p = \left(v_n^2 + v_t^2 \right)^{1/2} = \dot{q} \, [1 - x_e(\eta) \cos^2 \eta]^{1/2} \tag{57}$$

21. To obtain the projectile equation of motion for the case of a conical nose, Equation 53 is inserted into Equation 49, and the resulting expression for p_I is used in Equation 48. The total axial resisting force F_z acting on the projectile is then found according to

$$F_z = \int_{z=0}^{z=L} [p_s + p_I(z, \phi)] \sin \phi \; dA(z, \phi) \tag{58}$$

where the surface element $dA(z, \phi)$ is expressed as

$$dA(z, \phi) = 2\pi \, \frac{\tan \phi}{\cos \phi} \, z \; dz \tag{59}$$

Similarly, for an ogive nose, Equation 57 is inserted in Equation 49, and the resulting expression for p_I is used in Equation 48. Then F_z is found according to

$$F_z = \int_{\eta=\phi}^{\eta=0} [p_s + p_I(\eta)] \sin \eta \; dA(\eta) \tag{60}$$

where the surface element $dA(\eta)$ is expressed as

23

$$dA(\eta) = \frac{2\pi a_o^2(\cos \eta - \cos \phi)[(\cos \phi - \cos \eta) \cos^2 \eta - \cos \eta] \, d\eta}{(1 - \cos \phi)^2 \cos \eta} \tag{61}$$

For both cases, the projectile equation of motion is obtained by setting $M\ddot{q} = -F_z$, where M is the projectile mass. The resulting equation of motion has the form

$$\left(M + \pi a_o^3 \rho_\ell B_1\right)\ddot{q} = -\pi a_o^2\left(p_s + \rho_\ell B_2 f_n \dot{q}^2\right) \tag{62}$$

where p_s , B_1 , and B_2 are given by Equations 39-41 as functions of the target yield strength Y , elastic modulus E , strain-hardening modulus E_t , and compaction coefficient α . The quantity f_n is the so-called nose shape factor resulting from the variation of dynamic pressure along the projectile frontal surface. For conical noses, f_n is given by

$$f_n = \sin^2 \phi + \frac{1}{3} \cos^2 \phi \tag{63}$$

where ϕ is related to the nose length L and projectile diameter $D = 2a_o$ by

$$\tan \phi = \frac{D}{2L} \tag{64}$$

For ogives, the nose shape factor is

$$f_n = 1 - \frac{2}{\epsilon^2(1 - \epsilon)^6}\left[B^2 \ln (2 - \epsilon) - (3B^2 + 2B)(B - \epsilon)\right.$$

$$+ \frac{1}{2} (3B^2 + 6B + 1)(B^2 - \epsilon^2) - \frac{1}{5} (B^5 - \epsilon^5)$$

$$\left. - \frac{1}{3} (B^2 + 6B + 3)(B^3 - \epsilon^3) + \frac{1}{4} (2B + 3)(B^4 - \epsilon^4)\right] \tag{65}$$

where

$$B = 2\epsilon - \epsilon^2 \tag{66}$$

and the parameter ϵ is related to the ogive caliber radius (CRH) and to L/D by

$$CRH = \frac{R}{D} = \frac{1}{2\epsilon} = \frac{L^2}{D^2} + \frac{1}{4} \tag{67}$$

(A hemisphere is an ogive with $CRH = L/D = 1/2$, in which case Equation 65 reduces to $f_n = 2/3$.) As pointed out in Reference 5, Equation 62 is presumed to be valid only for projectiles and targets for which the condition $\pi a_o^3 \rho_\ell B_1 \ll M$ is satisfied. In any case, the term B_1 is thought to represent an upper limit insofar as the effect of target acceleration is concerned.

22. During the embedding of the nose (penetration depth $q \leq L$), the projectile equation of motion is obtained by substituting a_s for a_o in Equation 62, where a_s is the cylindrical radius of the projectile at the target surface.

23. For the penetration of layered targets, the quantities p_s , B_1 , and B_2 are modified in accordance with the cavity expansion theory for a concentrically layered medium. The derivation of these quantities in Reference 5 is lengthy and cumbersome; thus it is appropriate that the discussion for layered targets be deferred until later when a simpler approach will be taken in the development of the deep penetration theory.

Solid Reynolds Number

24. Among the various parameters defined in Reference 5 is the "solid Reynolds number," which is an order-of-magnitude index of the ratio of dynamic pressure (i.e., inertial stress) to shear stress in the target, defined by

$$R_s \equiv \frac{\rho_0 \dot{q}^2}{Y} \tag{68}$$

25

The solid Reynolds number can be used as a scaling parameter for experimental and theoretical results for cohesive targets and also as an indicator of the relative applicability of the shallow penetration theory to particular penetration problems. The working range of this theory for depth predictions appears to be $0 < R_s \leq 100$, while the working range for projectile deceleration predictions (accurate within a factor of two) is more like $0 < R_s \leq 10$. In other words, the shallow penetration theory seems to work best for cases in which the resistance of the target due to shear is comparable to that due to inertia. When the solid Reynolds number becomes very large (i.e., for "high" velocities and "soft" targets), the theory overpredicts the projectile deceleration, which results in an underprediction of the final penetration depth. Furthermore, the magnitudes of the overprediction and underprediction tend to increase with increasing R_s.

25. The breakdown of the shallow penetration theory at high values of R_s is not surprising since the dynamic pressure variation along the projectile frontal surface is obtained from a particle velocity distribution $v_p/\mathring{q}$, which is a function only of projectile geometry and axial distance from the nose tip. This results in a nose shape factor or "drag coefficient" which is a function of projectile geometry alone and which is independent of projectile velocity and target properties. In order to account for the variation of f_n with projectile geometry, projectile velocity, and target properties, an approach is now sought that will yield f_n as a function of the solid Reynolds number as well as the projectile geometry.

Deep Penetration Theory for Homogeneous Targets

26. In attempting to develop a penetration theory which is applicable at high values of R_s, one might modify any or all of the basic assumptions of the shallow penetration theory (see paragraph 17). In particular, the assumption of complete contact between the target and the projectile frontal surface is questionable, and the possible occurrence of separation on the frontal surface may affect the resistance of

the target to penetration. Nevertheless, all of the basic assumptions of the shallow penetration theory will be retained, and the development of the deep penetration theory will proceed from a simple modification of the particle velocity distribution on the projectile frontal surface.

27. The constraints on particle motion along the frontal surface (see paragraph 19) are taken to be the same as in the shallow penetration theory, except for the assumption that $v_t = 0$ at the base of the nose. This particular constraint is relaxed to allow more flexibility in the distribution of v_t along the frontal surface.

28. Considering first a projectile with a fully embedded conical nose as shown in Figure 3, the particle velocity component v_n, normal to the frontal surface, is still given by Equation 50. However, the tangential velocity component v_t is now assumed to vary according to

$$v_t(x, R_s) = (\dot{q} \cos \phi)e^{-\psi(R_s)x^2/2} \tag{69}$$

where $x = z/L$, $R_s = \rho_0\dot{q}^2/Y$, and $\psi(R_s)$ is an unknown function of R_s. Equation 69 is by no means a unique expression for v_t. It does, however, represent a convenient functional form in which v_t decreases with increasing x and increasing ψ. If $\psi(R_s)$ is chosen to be a monotonically increasing function, then Equation 69 will result in an expression for the nose shape factor or "drag coefficient" that decreases with increasing projectile velocity and nose length (which is more or less consistent with experimental observation). Incorporating Equation 69 (which now replaces Equation 51) in Equation 53, the expression for v_p becomes

$$v_p = \dot{q}\left[\sin^2 \phi + \cos^2 \phi \, e^{-\psi(R_s)x^2}\right]^{1/2} \tag{70}$$

Equation 70 is substituted into Equation 49, which is in turn inserted into Equation 58. Setting $M\ddot{q} = -F_z$ as before, the resulting projectile equation of motion is

$$\left(M + \pi a_o^3 \rho_\ell B_1\right)\ddot{q} = -\pi a_o^2 \left[p_s + \rho_\ell B_2 f_n(\phi, R_s)\dot{q}^2\right] \qquad (71)$$

where

$$f_n(\phi, R_s) = \sin^2 \phi + \frac{1 - e^{-\psi(R_s)}}{\psi(R_s)} \cos^2 \phi \qquad (72)$$

Equation 72 now replaces Equation 63 for the nose shape factor f_n during all phases of the penetration process, including the embedding of the nose.

29. Equation 72 is, of course, restricted to projectiles with conical nose shapes. In order to apply the present approach directly to ogives, Equation 69 should be replaced by

$$v_t(\eta, R_s) = (\dot{q} \cos \eta)e^{-\psi(R_s)x_e^2(\eta)/2} \qquad (73)$$

where η is defined in Figure 4, and $x_e(\eta)$ is given by Equation 55. Equation 73 should then be used in the relation $v_p^2 = v_n^2 + v_t^2$ which is in turn substituted into Equation 49. The resulting equation for the dynamic pressure p_I must then be inserted into Equation 60 to obtain the resisting force F_z and, subsequently, the projectile equation of motion which will be of the same form as Equation 71 but with an extremely complicated relation among f_n, ψ, and the maximum half-angle ϕ (Figure 4). Moreover, the integral for F_z must be evaluated numerically when this approach is taken, and thus it is expedient to seek a simpler approach that results in an approximate analytic expression for f_n.

30. In order to obtain an expression for f_n which has the same form as Equation 72, the effective ogive half-angle is defined as follows:

$$\sin^2 \phi_e \equiv \frac{\displaystyle\int_{\eta=\phi}^{\eta=0} \sin^2 \eta \; dA(\eta) \sin \eta}{\displaystyle\int_{\eta=\phi}^{\eta=0} dA(\eta) \sin \eta} \tag{74}$$

where

$$\cos^2 \phi_e = 1 - \sin^2 \phi_e \tag{75}$$

and $dA(\eta)$ is given by Equation 61. Evaluation of Equation 74 results in

$$\sin^2 \phi_e = \frac{3 - 8 \cos \phi + 6 \cos^2 \phi - \cos^4 \phi}{6 - 12 \cos \phi + 6 \cos^2 \phi} \tag{76}$$

where ϕ is the maximum value of η, and ϕ is related to CRH and L/D by

$$\cos \phi = 1 - \frac{1}{2 \cdot CRH} = \frac{4(L^2/D^2) - 1}{4(L^2/D^2) + 1} \tag{77}$$

The nose shape factor for ogives is then approximated by

$$f_n(R_s, \phi_e) \cong \sin^2 \phi_e + \frac{1 - e^{-\psi(R_s)}}{\psi(R_s)} \cos^2 \phi_e \tag{78}$$

According to this scheme, any ogive can be replaced by its equivalent cone which, by definition, has approximately the same value of f_n as the ogive. Equivalent cone L/D ratios are listed for ogives in Table 1.

31. At this point only the relation between ψ and R_s is still unspecified. In accordance with paragraph 28, ψ is defined as a monotonically increasing function of R_s with the limiting values

$$\lim_{R_s \to 0} \psi = 0 \tag{79}$$

and

$$\lim_{R_s \to \infty} \psi = \infty \tag{80}$$

Table 1

Equivalent Cone Parameters for Ogives

Ogive CRH	Ogive L/D	Equivalent Cone L/D	Ogive CRH	Ogive L/D	Equivalent Cone L/D
0.5	0.50	0.50	5.5	2.29	1.99
1.0	0.87	0.78	6.0	2.40	2.08
1.5	1.12	0.99	6.5	2.50	2.17
2.0	1.32	1.16	7.0	2.60	2.26
2.5	1.50	1.31	7.5	2.69	2.34
3.0	1.66	1.45	8.0	2.78	2.42
3.5	1.80	1.57	8.5	2.87	2.50
4.0	1.94	1.69	9.0	2.96	2.57
4.5	2.06	1.80	9.5	3.04	2.64
5.0	2.18	1.90	10.0	3.12	2.71

The corresponding limiting values for f_n are then

$$\lim_{R_s \to 0} f_n = 1 \tag{81}$$

with

$$\lim_{R_s \to \infty} f_n = \sin^2 \phi \tag{82}$$

30

for cones and

$$\lim_{R_s \to \infty} f_n = \sin^2 \phi_e \tag{83}$$

for ogives. It now remains to determine a single monotonically increasing function $\psi(R_s)$ which satisfies Equations 79 and 80 and which results in acceptable predictions of projectile deceleration and final penetration depth. This function must be determined empirically, but once established it will be considered "universal," i.e., it will be presumed to be the same for all projectiles and all cohesive targets, within the context of the present theory. If a different function $\psi(R_s)$ has to be chosen for each target and each projectile, then the theory is no better than a strictly empirical approach in which the "constants" in the projectile equation of motion must be determined separately for each individual situation. On the other hand, if a single function $\psi(R_s)$ can be found that correlates experimental data for a variety of projectiles and targets, for both shallow and deep penetration, then the theory may represent a useful tool for making predictions before the fact.

32. With the preceding observations in mind, the following equation is proposed for $\psi(R_s)$:

$$\psi(R_s) = \left(\frac{R_s}{8}\right)^{3/4} \tag{84}$$

It will be shown in Part IV that Equation 84 results in good agreement between theory and experiment for a number of different projectiles and targets. Other expressions for $\psi(R_s)$ have been found that also produce good results (e.g., $\psi = R_s/15$), but Equation 84 appears to produce the best overall results within the context of the present theory.

Deep Penetration Theory for Layered Targets

33. In order to modify the projectile equation of motion (71) for

31

the penetration of layered targets, the appropriate expressions for the quantities p_s, B_1, and B_2 must first be determined by means of an analogy with dynamic cavity expansion in a concentrically layered medium. The situation to be considered is illustrated in Figure 5;
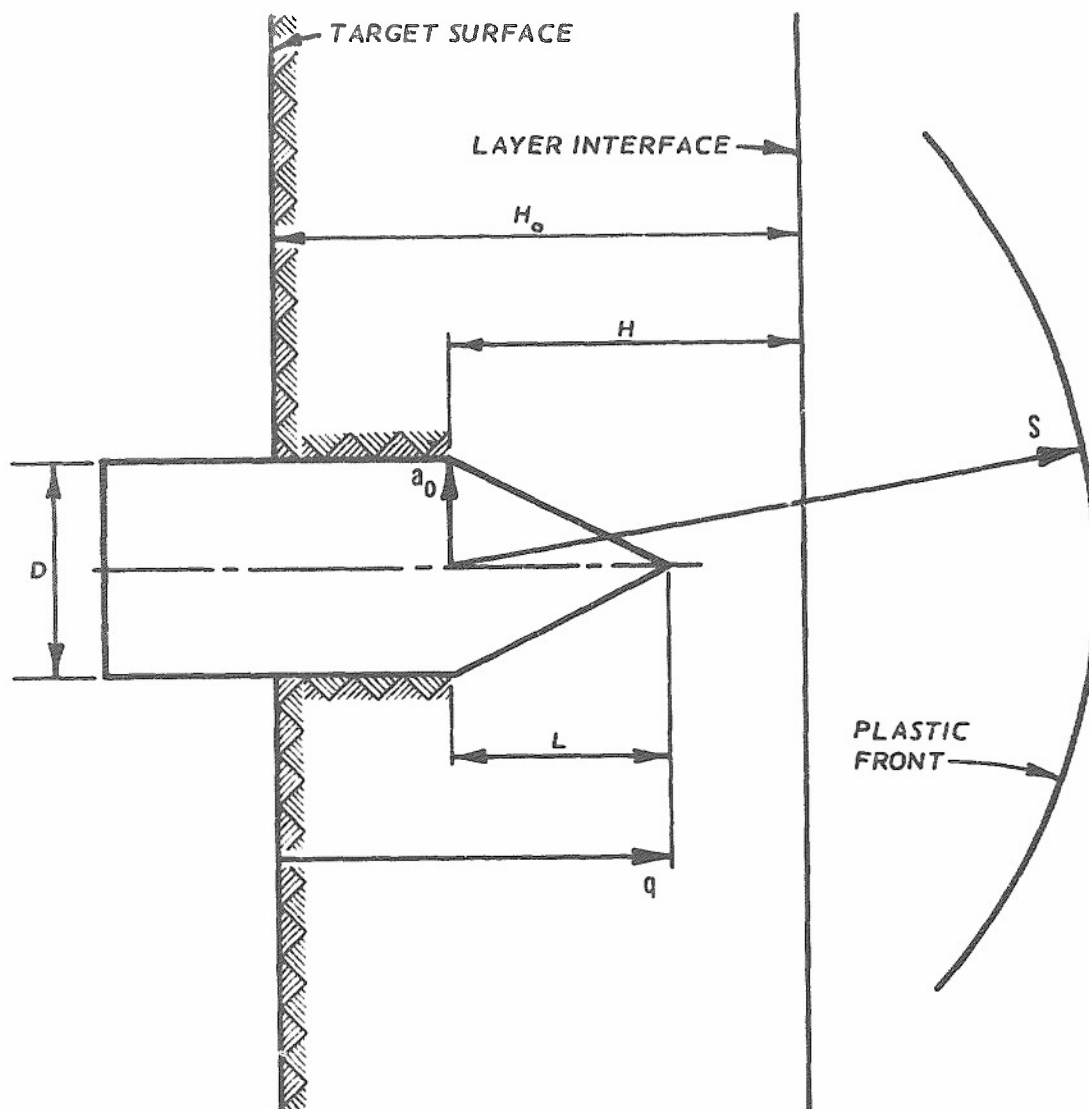

Figure 5. Projectile penetration in a layered target

however, the target may have any number of layers as long as the projectile motion is significantly influenced by only two layers at a time. The penetration process is now divided into two regimes: (a) when $L < H$, the nose tip has not yet reached the layer interface; and (b) when $L \geq H$, the projectile has begun to perforate the layer interface. Each of these regimes can be divided into three subregimes: (a) when $S < H$, the plastic front has not yet reached the layer

interface; (b) when $S \geq H$, the plastic front has reached the layer interface; and (c) when $H \leq a_o$, the effect of the first layer on the projectile equation of motion is negligible.

34. To approximate the values of p_s, B_1, and B_2 for the above regimes and subregimes, it is first necessary to consider Equations 30-41 in Part II. In Reference 5, an attempt is made to account for the deformation of the layer interface due to the approaching projectile. Moreover, an upper limit approximation is used to obtain the effective interface deformation, and the resulting expressions for H, S, p_s, B_1, and B_2 are not only lengthy and cumbersome, but the approximation for the interface deformation is itself questionable and has only a small effect on the actual values of p_s, B_1, and B_2. A great deal of complication can then be avoided (without any demonstrable loss of accuracy) by simply neglecting the deformation of the interface altogether. Accordingly, the quantities $h(t)$ and h_o which appear in Equations 32-37 will be replaced by the distance H from the base of the projectile nose to the interface,

$$H = H_o - q + L \tag{85}$$

As a result, the criteria $L < H$ and $L \geq H$ can now be replaced by $q < H_o$ and $q \geq H_o$, respectively.

35. In the first regime where $q < H_o$, the equations for p_s, B_1, and B_2 are obtained by replacing $a(t)$ with a_o, $h(t)$ and h_o with H, and $b(t)$ with S (effective distance from base of projectile nose to plastic front) in Equations 23, 29, and 32-37. Then, $S < H$ is substituted for the criterion $b < h_o$. The results are as follows:

$$S^3 \cong \frac{a_o^3}{\delta_1} , \quad S < H \tag{86}$$

33

$$p_s(S < H) = -\frac{2}{3} Y_1 \ln \delta_1 + \frac{4}{9} E_{t1}\left(\frac{\pi^2}{6} - \sum_{m=1}^{\infty} \frac{\delta_1^m}{m^2}\right)$$

$$+ \frac{4}{3} \beta_1 E_1\left(1 - \frac{S^3}{H^3}\right) + \frac{4}{3} \beta_2 E_2 \frac{S^3}{H^3} \qquad (87)$$

$$B_1(S < H) = 1 - \delta_1^{1/3} + \left(1 - \frac{\alpha}{\delta_1}\right)\left[\delta_1^{1/3} - \left(1 - \frac{\rho_{02}}{\rho_{01}}\right)\frac{a_o}{H}\right] \qquad (88)$$

$$B_2(S < H) = 2B_1 + \frac{\alpha(1 - \delta_1)^2}{\delta_1^{2/3}(1 - \alpha)} - \frac{1}{2}\left(1 - \delta_1^{4/3}\right)$$

$$- \frac{\left(1 - \frac{\alpha}{\delta_1}\right)^2}{2(1 - \alpha)}\left[\delta_1^{4/3} - \left(1 - \frac{\rho_{02}}{\rho_{01}}\right)\frac{a_o^4}{H^4}\right] \qquad (89)$$

$$S^3 \cong \frac{a_o^3}{\delta_2} + \left(1 - \frac{\delta_1}{\delta_2}\right)H^3 \ , \ S \geq H \qquad (90)$$

$$p_s(S \geq H) = 2Y_1 \ln \frac{H}{a_o} + \frac{4}{9} E_{t1}\left[\frac{\pi^2}{6} - \sum_{m=1}^{\infty} \frac{(a_o/H)^{3m}}{m^2}\right]$$

$$+ 2Y_2 \ln \frac{S}{H} + \frac{4}{9} E_{t2} \sum_{m=1}^{\infty} \frac{1}{m^2}\left[\left(\frac{a_o}{H}\right)^{3m} - \left(\frac{a_o}{S}\right)^{3m}\right]$$

$$+ \frac{4}{3} \beta_2 E_2 \qquad (91)$$

$$B_1(S \geq H) = 1 - \left(1 - \frac{\rho_{02}}{\rho_{01}}\right)\frac{a_o}{H} - \frac{\alpha \rho_{02} a_o}{\delta_2 \rho_{01} S} \qquad (92)$$

34

$$B_2(S \geq H) = 2B_1 + \frac{\alpha \left(\frac{\rho_{02}}{\rho_{01}}\right)(1 - \delta_2)^2 \left(\frac{a_o^4}{S^4}\right)}{\delta_2^2(1 - \alpha)}$$

$$- \frac{1}{2}\left[1 - \frac{a_o^4}{H^4} + \frac{\rho_{02}}{\rho_{01}}\left(\frac{a_o^4}{H^4} - \frac{a_o^4}{S^4}\right)\right]$$

$$- \frac{1}{2}\frac{\left(\frac{a_o^4}{S^4}\right)\left(\frac{\rho_{02}}{\rho_{01}}\right)\left(1 - \frac{\alpha}{\delta_2}\right)^2}{1 - \alpha} \tag{93}$$

Thus, when $q < H_o$, $\rho_{\ell 1}$ is substituted for ρ_ℓ in the projectile equation of motion (71), and the expressions for p_s , B_1 , and B_2 are replaced, respectively, by Equations 87-89 when $S < H$ and by Equations 91-93 when $S \geq H$. The quantity α is the composite compaction coefficient for the two layers (which will be discussed later); δ_1 and δ_2 are defined by Equation 24; and, with the exception of B_1 and B_2 , the subscripts "1" and "2" denote quantities evaluated in the first and second layers, respectively. In the regime $q < H_o$, the effective nose shape factor f_{n*} is approximated according to

$$f_{n*} = \left(1 - \frac{a_o}{H}\right)f_{n1} + \frac{a_o}{H}f_{n2} \tag{94}$$

where f_{n1} and f_{n2} are obtained by inserting $R_{s1} = \rho_{01}\dot{q}^2/Y_1$ and $R_{s2} = \rho_{02}\dot{q}^2/Y_2$, respectively, into the equation for f_n . Thus, when $q < H_o$, then $f_n = f_{n*}$ and the product $f_n B_2$ is given by

$$f_n B_2 = f_{n*}B_2(S < H) \ , \ S < H \tag{95.}$$

$$f_n B_2 = f_{n*}B_2(S \geq H) \ , \ S \geq H \tag{96}$$

When $a_o = H$, Equation 94 reduces to $f_{n*} = f_{n2}$, Equation 90 becomes

35

approximately

$$S^3 \cong \frac{a_o^3}{\delta_2} \ , \quad a_o = H \tag{97}$$

and Equations 87-89 and 91-93 give way to Equations 39-41. (That is, the projectile equation of motion is the same as for a homogeneous target which has the same properties as the second layer). Accordingly, when $H \leq a_o$, ρ_ℓ is replaced in Equation 71 by $\rho_{\ell 2}$ and p_s , B_1, and B_2 are written as

$$p_s(H \leq a_o) = -\frac{2}{3} Y_2 \ln \delta_2 + \frac{4}{9} E_{t2} \left(\frac{\pi^2}{6} - \sum_{m=1}^{\infty} \frac{\delta_2^m}{m^2} \right) + \frac{4}{3} \beta_2 E_2 \tag{98}$$

$$B_1(H \leq a_o) = 1 - \frac{\alpha}{\delta_2^{2/3}} \tag{99}$$

$$B_2(H \leq a_o) = \frac{3}{2} - \frac{\alpha}{\delta_2^{2/3}} \left[2 - \frac{(1 - \delta_2)^2}{1 - \alpha} \right]$$

$$+ \frac{1}{2} \delta_2^{4/3} \left[1 - \left(1 - \frac{\alpha}{\delta_2} \right)^2 (1 - \alpha) \right] \tag{100}$$

36.   In the other regime where $q \geq H_o$, the expressions for p_s , B_1 , and $f_n B_2$ when $S < H$ are approximated by

$$p_s \cong \left(1 - \frac{a_I^2}{a_o^2} \right) p_s(S < H) + \frac{a_I^2}{a_o^2} p_s(H \leq a_o) \tag{101}$$

$$B_1 \cong \left(1 - \frac{a_I^3}{a_o^3} \right) B_1(S < H) + \frac{\rho_{02} a_I^3}{\rho_{01} a_o^3} B_1(H \leq a_o) \tag{102}$$

$$f_n B_2 \cong \left(1 - \frac{a_I^2}{a_o^2} \right) f_{n*} B_2(S < H) + \frac{\rho_{02} a_I^2}{\rho_{01} a_o^2} f_{n2} B_2(H \leq a_o) \tag{103}$$

where a_I is the cylindrical radius of the projectile at the interface location H_O, and S is still given by Equations 90 and 95. The conditions $S < H$ and $q \geq H_O$ can occur simultaneously only when $L > S$, i.e., when the projectile nose length is greater than the effective radius of the plastic front relative to the base of the nose. On the other hand, when $S \geq H$, p_s, B_1, and $f_n B_2$ are approximated by

$$p_s \cong \left(1 - \frac{a_I^2}{a_o^2}\right) p_s(S \geq H) + \frac{a_I^2}{a_c^2} \, p_s(H \leq a_o) \tag{104}$$

$$B_1 \cong \left(1 - \frac{a_I^3}{a_o^3}\right) B_1(S \geq H) + \frac{\rho_{02} a_I^3}{\rho_{01} a_o^3} B_1(H \leq a_o) \tag{105}$$

$$f_n B_2 \cong \left(1 - \frac{a_I^2}{a_o^2}\right) f_{n*} B_2(S \geq H) + \frac{\rho_{02} a_I^2}{\rho_{01} a_o^2} \, f_{n2} B_2(H \leq a_o) \tag{106}$$

For both regimes (i.e., $q < H_O$ and $q \geq H_O$) the expressions for p_s, B_1, and B_2 reduce to Equations 98-100 when $a_o = H$. Thus, whenever $H \leq a_o$, the projectile equation of motion is Equation 71 with $\rho_\ell = \rho_{\ell 2}$, $f_n = f_{n2}$, and p_s, B_1, and B_2 given by Equations 98-100, respectively.

Target Compressibility

37. In order to estimate the target compaction coefficient α at any time during the penetration process, an estimate is first made for the volume-averaged dynamic pressure P_{ave} in the plastic zone surrounding the projectile frontal surface.[5] This is done by substituting $\dot{q}$ for $\dot{a}$ in Equation 42 and dropping the acceleration term (projectile acceleration is always negative and could result in a negative value of P_{ave}, which is inadmissible). The resulting equation is multiplied by f_n to account for the effect of nose shape at high values of R_s, and one then obtains

$$P_{ave} \cong \frac{3}{2} \rho_0 f_n \dot{q}^2 \left[2(3\beta)^{1/3} - 9\beta + 3(3\beta)^{4/3} \right] \qquad (107)$$

This equation is used in a pressure-density relation (e.g., Equation 44) to estimate α. For layered targets, α is calculated separately for each layer, and then a composite value is determined by substituting a_o for $a(t)$ and H for $h(t)$ in Equation 45 yielding

$$\alpha = \alpha_1 \left(1 - \frac{a_o}{H} \right) + \alpha_2 \frac{a_o}{H} \quad, \quad a_o \leq H \qquad (108)$$

Oblique Impact

38. No modifications have been made in the oblique impact theory, which is discussed in Reference 5. The oblique theory is still limited to predictions of projectile rotation during the embedding of the nose and is yet to be verified by comparison with experiment. However, in light of the present work, it is appropriate to replace the value of f_n used in Reference 5 with that given by Equation 72. Thus, the equations which govern the forces and moments acting on the projectile will have the same form as before, but the incorporation of Equation 72 for f_n introduces an implicit dependence upon the solid Reynolds number. Since f_n is a decreasing function of R_s, maximum projectile rotation will be seen at low values of R_s, and the projectile rotation will be a more rapidly decreasing function of impact velocity than that produced by the value of f_n which was used in Reference 5.

Nondimensional Results for Typical Targets

39. Although the penetration theory which has been developed may appear somewhat complicated at first, the implications for homogeneous targets are fairly simple when viewed in the proper perspective. For heavy projectiles (i.e., $\pi a_o^3 \rho_\ell B_1 \ll M$), the projectile equation of motion reduces approximately to

$$\ddot{M\ddot{q}} \cong \begin{cases} -\pi a_s^2 \left[p_s + \rho_\ell B_2 f_n \dot{q}^2 \right] , & q < L \\[2em] -\pi a_o^2 \left[p_s + \rho_\ell B_2 f_n \dot{q}^2 \right] , & q \geq L \end{cases} \tag{109}$$

which can be replaced by

$$-\frac{M\ddot{q}}{\pi a_o^2 p_s} \cong \begin{cases} \dfrac{a_s^2}{a_o^2} \left(1 + \dfrac{\rho_\ell B_2 f_n \dot{q}^2}{p_s} \right) , & q < L \\[2em] 1 + \dfrac{\rho_\ell B_2 f_n \dot{q}^2}{p_s} , & q \geq L \end{cases} \tag{110}$$

For slightly compressible targets, the range of values for $\rho_\ell B_2$ is

$$\rho_0 \leq \rho_\ell B_2 \leq \frac{3}{2} \rho_0 \tag{111}$$

and the corresponding range for p_s is

$$2Y \leq p_s \leq 5Y \tag{112}$$

It is reasonable to characterize a "typical" target by $p_s \cong 4Y$ and $\rho_\ell B_2 \dot{q}^2 / p_s \cong \frac{1}{3} R_s$, so that Equation 110 becomes

$$-\frac{M\ddot{q}}{\pi a_o^2 p_s} \cong \begin{cases} -\dfrac{M\ddot{q}}{4\pi a_o^2 Y} \cong \dfrac{a_s^2}{a_o^2} \left(1 + \dfrac{1}{3} f_n R_s \right) , & q < L \\[2em] -\dfrac{M\ddot{q}}{4\pi a_o^2 Y} \cong 1 + \dfrac{1}{3} f_n R_s , & q \geq L \end{cases} \tag{113}$$

When the transformation

$$\ddot{q} = \frac{1}{2} \frac{d}{dq} (\dot{q}^2) \tag{114}$$

39

and the nondimensional depth

$$\xi = \frac{8\pi a_o^2 \rho_0 q}{M} \tag{115}$$

are introduced, Equation 113 gives way to

$$-\frac{M\ddot{q}}{\pi a_o^2 p_s} \cong \begin{cases} -\dfrac{dR_s}{d\xi} \cong \xi^2 \left(\dfrac{M}{8\pi a_o^2 \rho_0 L}\right)^2 \left(1 + \dfrac{1}{3} f_n R_s\right), & q < L \\[2em] -\dfrac{dR_s}{d\xi} \cong 1 + \dfrac{1}{3} f_n R_s , & q \geq L \end{cases} \tag{116}$$

For deep penetration (final penetration depth $q_f \gg L$), Equation 116 can be replaced by

$$-\frac{M\ddot{q}}{\pi a_o^2 p_s} \cong -\frac{dR_s}{d\xi} \cong 1 + \frac{1}{3} f_n R_s \tag{117}$$

The peak nondimensional deceleration of the projectile can thus be obtained by using the impact value of $R_s = \rho_0 v_o^2/Y$, and the corresponding dimensional value is obtained by multiplying by $4\pi a_o^2 Y/M$. The final nondimensional penetration depth $\xi_f = 8\pi a_o^2 \rho_0 q_f/M$ is found by integrating Equation 117 numerically, and the corresponding dimensional depth is found by multiplying ξ_f by $M/8\pi a_o^2 \rho_0$. In Figure 6, peak nondimensional deceleration is plotted against nondimensional impact velocity $v_o\sqrt{\rho_0/Y}$ for conical noses with $L/D = 1$, 2, and 3 . In Figure 7, nondimensional final penetration depth is plotted against nondimensional impact velocity. Results are presented for the shallow penetration theory, in which $f_n = f_n(\phi)$, and for the deep penetration theory, in which $f_n = f_n(\phi, R_s)$. For very blunt noses, i.e., $L/D \leq 1/2$, the predictions of the deep penetration theory reduce essentially to those of the shallow penetration theory. Thus, it is emphasized that at high values of R_s deep penetration theory is probably valid only for sharp projectiles where $L/D \geq 1$. A deep penetration
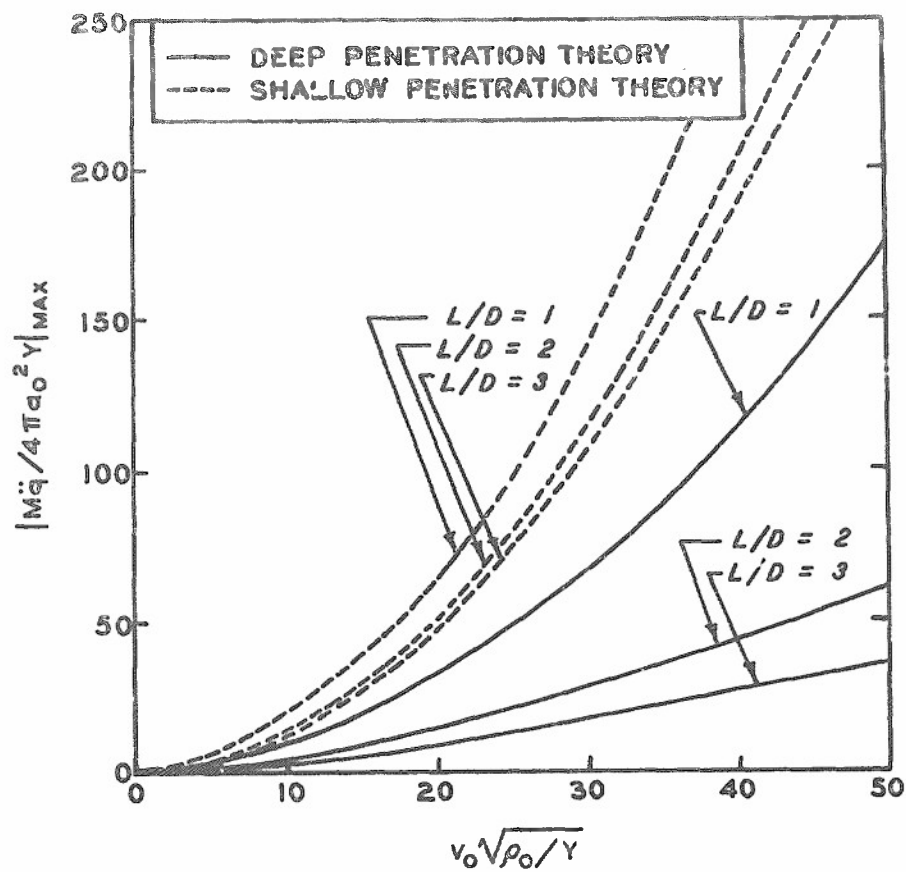
Figure 6. Nondimensional peak deceleration versus impact velocity for conical projectiles and "typical" targets
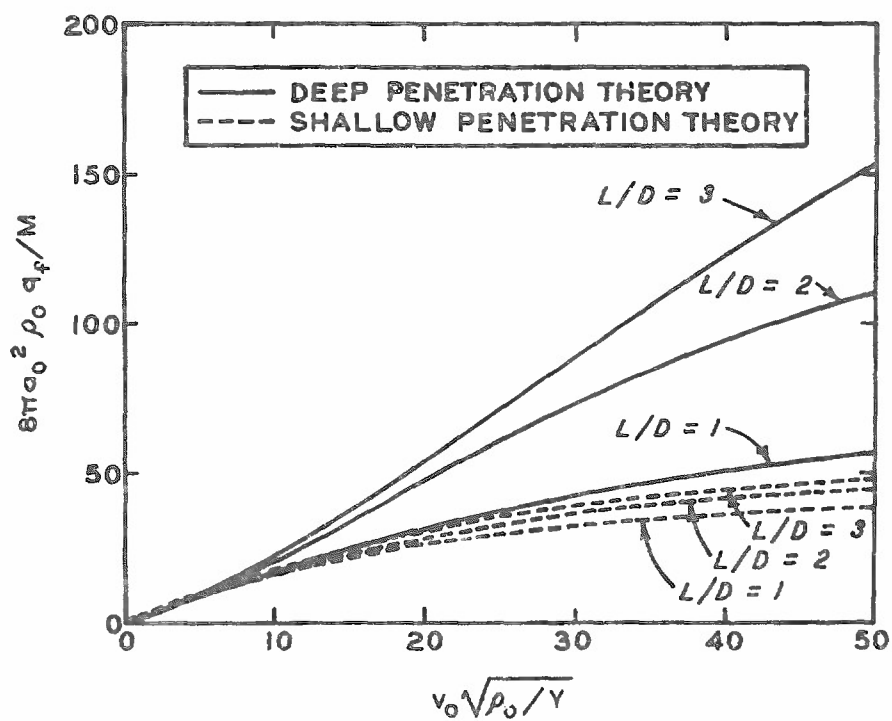

Figure 7. Nondimensional final penetration depth versus impact velocity for conical projectiles and "typical" targets

41

theory for blunt projectiles should account for the effect of target
material just ahead of the projectile which is formed into a sharp coni-
cal "nose" during the impact phase.

PART IV: APPLICATIONS

Introduction

40.   This part of the report is devoted to the application of the
deep penetration theory to problems of practical interest and to the
comparison of theoretical results with experimental, empirical, and 2D
finite-difference results for cohesive targets. In the applications
which follow, the range of the solid Reynolds number extends from very
low values (shallow penetration) to very high values (deep penetration),
and the function $\Psi(R_s)$ is given by Equation 84 for __all__ targets and __all__
projectiles. In each example, the predictions of the shallow penetra-
tion theory are compared with those of the deep penetration theory.
When comparisons are shown with 2D finite-difference calculations, no
attempt is made to assess the validity or accuracy of the various as-
sumptions and techniques employed by different authors since this lies
beyond the scope of the present investigation. Thus, the reasons for
agreement or disagreement between theoretical and 2D solutions remain
open to speculation. The agreement achieved between theoretical predic-
tions and empirical and experimental results is encouraging but not
conclusive. Furthermore, the relative applicability or inapplicability
of the deep penetration theory to the overall range of practical problems
can only be demonstrated by extensive comparison with experimental data
from deep penetration tests. However, most data which are now available
lie in the range of shallow to moderate depths for which the theory is
already fairly well documented.

Choice of Material Properties

41.   The development of the deep penetration theory stems from
the cavity expansion theory which is based upon the presumption of rate-
independent, bilinear material behavior in shear. Unfortunately, real
materials exhibit neither bilinear shear behavior nor rate-independence,
and so there exists the problem of choosing an appropriate bilinear

43

stress-strain curve that adequately approximates real material behavior insofar as it relates to cavity expansion and projectile penetration. For upper-bound predictions of final penetration depth, the results of unconfined static triaxial compression tests are used to estimate target shear properties; and for many applications, these upper-bound predictions are adequate. However, for a priori predictions in untried targets, upper-bound predictions should be supplemented with lower-bound predictions using properties obtained from the results of dynamic tests. Anisotropic behavior may further complicate the situation so that upper- and lower-bound properties have to be chosen with regard to maximum variation due to anisotropy as well as rate effects. In any case, acceptable results are usually obtained by setting $E_t = 0$ and idealizing the "real" stress-strain curve, as shown in Figure 8.
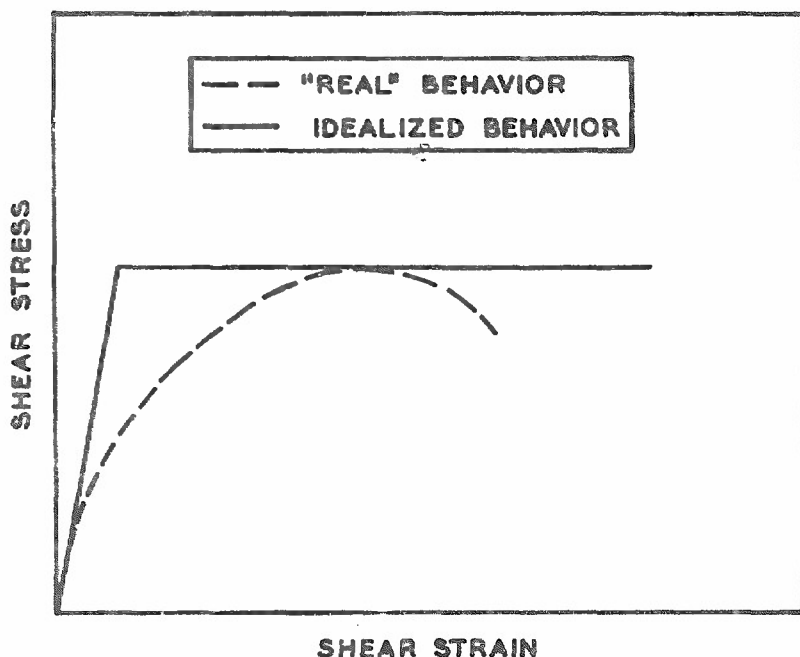

Figure 8. Idealization of a "real" stress-strain curve

Shallow Penetration of Rock

42. Thigpen[6] has performed 2D finite-difference calculations in an attempt at simulating two rock penetration tests reported by Patterson.[7] In these calculations the shallow penetration of nonrigid frictionless projectiles in Madera limestone and welded tuff is analyzed

using an elastic-plastic Von Mises material model for both target and projectile. The predictions of the shallow and deep penetration theories are now compared with the 2D results for rigid but otherwise identical projectiles. For the range of dynamic pressures encountered, the compressibility of both targets is adequately characterized by Equation 44, and the elastic modulus is approximately equal to the initial value. In the limestone calculation, the target properties used by Thigpen are

$$\rho_0 = 168 \text{ pcf* } (2.69 \text{ gm/cm}^3)$$

$$Y = 13{,}690 \text{ psi } (0.944 \text{ kbar})$$

$$E \cong 3.15 \times 10^6 \text{ psi } (217 \text{ kbar})$$

$$E_t = 0$$

$$C = 11{,}155 \text{ fps } (3400 \text{ m/sec})$$

and the (rigid) projectile characteristics are

$$W = 674 \text{ lb } (306 \text{ kg})$$

$$D = 8 \text{ in. } (20.32 \text{ cm})$$

$$CRH = 9.25 \text{ (ogive nose, } L/D = 3)$$

$$v_o = 570 \text{ fps } (174 \text{ m/sec})$$

where

ρ_0 = initial density

Y = compressive yield strength

E = elastic modulus

E_t = strain-hardening modulus

C = dilatational wave velocity

W = weight

D = diameter

CRH = ogive caliber radius

---

* A table of factors for converting U. S. customary units of measurement to metric (SI) units is presented on page 3.

L = nose length

v_o = impact velocity

In the welded tuff calculation, the target properties used by Thigpen are

$$\rho_0 = 115 \text{ pcf } (1.85 \text{ gm/cm}^3)$$

$$Y = 5510 \text{ psi } (0.380 \text{ kbar})$$

$$E \cong 1.09 \times 10^6 \text{ psi } (75.5 \text{ kbar})$$

$$E_t = 0$$

$$C = 6725 \text{ fps } (2050 \text{ m/sec})$$

and the (rigid) projectile characteristics are

$$W = 1000 \text{ lb } (455 \text{ kg})$$

$$D = 9 \text{ in. } (22.9 \text{ cm})$$

$$CRH = 6.0 \text{ (ogive nose, } L/D = 2.4$$

$$v_o = 695 \text{ fps } (212 \text{ m/sec})$$

The solid Reynolds numbers at impact are $R_s = 0.86$ and 2.17 in the limestone and tuff, respectively. The results are compared in Figures 9 and 10, showing that, for low values of R_s, the deep penetration theory predicts slightly higher decelerations and shallower final penetration depths than the shallow penetration theory. (This trend is reversed at high values of R_s.) As pointed out in Reference 6, the oscillations in the 2D results are due to projectile nonrigidity which is accounted for in neither the shallow nor deep penetration theories. No experimental deceleration record is available for the welded tuff test.

Shallow Penetration of a Hypothetical Frozen Soil

43. Ito et al.[8] have performed a 2D finite-difference calculation analyzing the penetration of a hypothetical frozen soil by a rigid projectile. The 2D calculation incorporates an elastic-plastic material
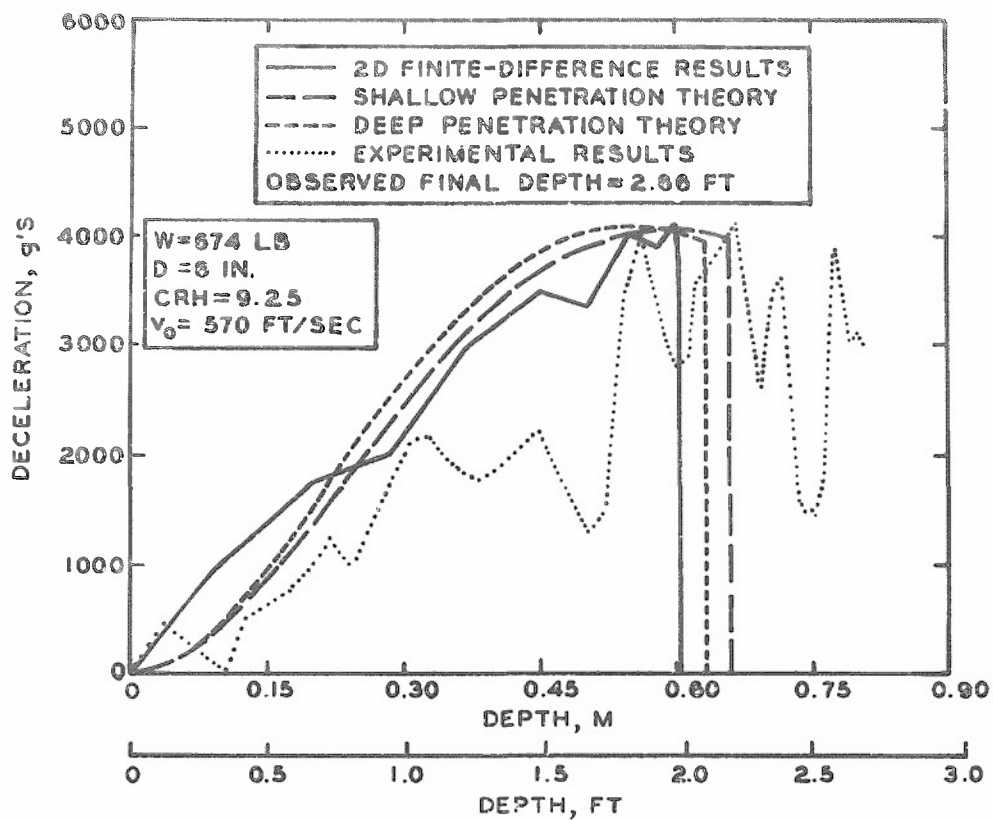
46

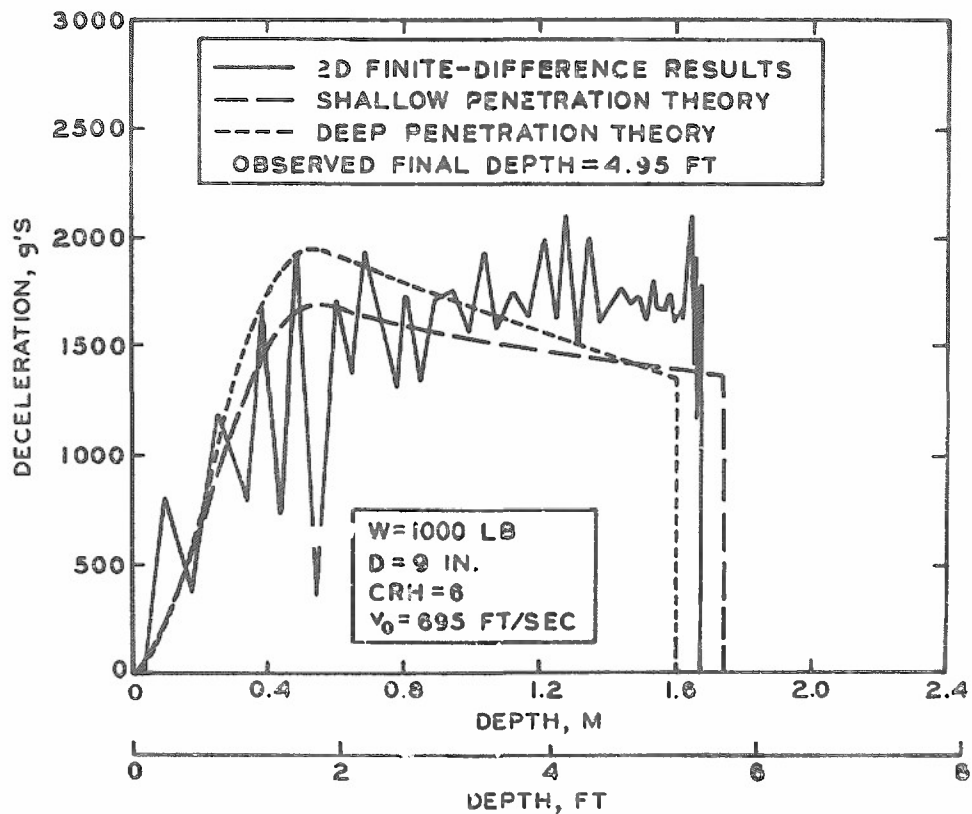Figure 9. Projectile deceleration versus depth
in Madera limestone

Figure 10. Projectile deceleration versus depth
in welded tuff

model with a Mohr-Coulomb yield surface as well as a hypothetical model for Coulomb friction in which the tangential stress at the projectile surface is proportional to the normal stress. By subtracting the contribution due to tangential stress from the net force on the projectile, it is possible to approximate the projectile loading for the "frictionless" case in addition to that for the hypothetical frictional case. The unconfined target properties are

$$\rho_0 = 125 \text{ pcf } (2.00 \text{ gm/cm}^3)$$

$$Y = 2030 \text{ psi } (0.140 \text{ kbar})$$

$$E = 5.70 \times 10^5 \text{ psi } (39.3 \text{ kbar})$$

$$E_t = 0$$

and

$$C \cong 7100 \text{ fps } (2165 \text{ m/sec})$$

Target compressibility is adequately characterized by Equation 44 for the range of dynamic pressures encountered. The projectile characteristics are

$$W = 17.3 \text{ lb } (7.86 \text{ kg})$$

$$D = 3 \text{ in. } (7.62 \text{ cm})$$

$$CRH = 2.35 \text{ (ogive nose, L/D = 1.45)}$$

and

$$v_o = 450 \text{ fps } (137 \text{ m/sec})$$

The shallow and deep penetration theories are now applied to the same problem (in the absence of friction), and the results are compared in Figures 11 and 12. The solid Reynolds number at impact is $R_s = 2.69$, and both theories produce peak decelerations and final penetration depths that are in approximate agreement with the 2D results for the "frictionless" case.

Shallow Penetration of Aluminum

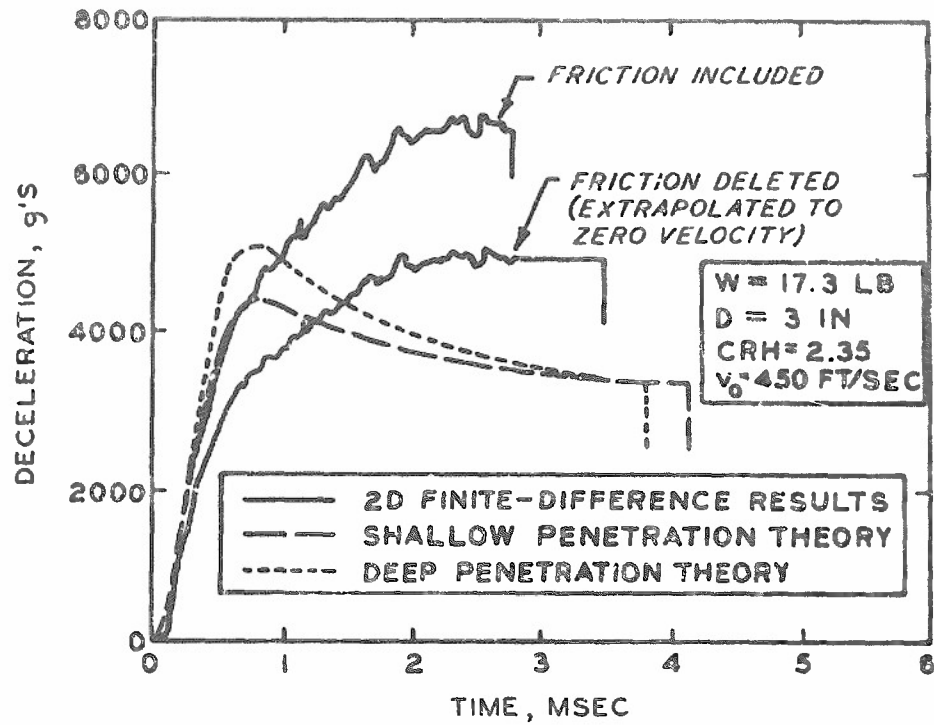44. Since the cavity-expansion-based penetration theory has

Figure 11. Projectile deceleration versus time
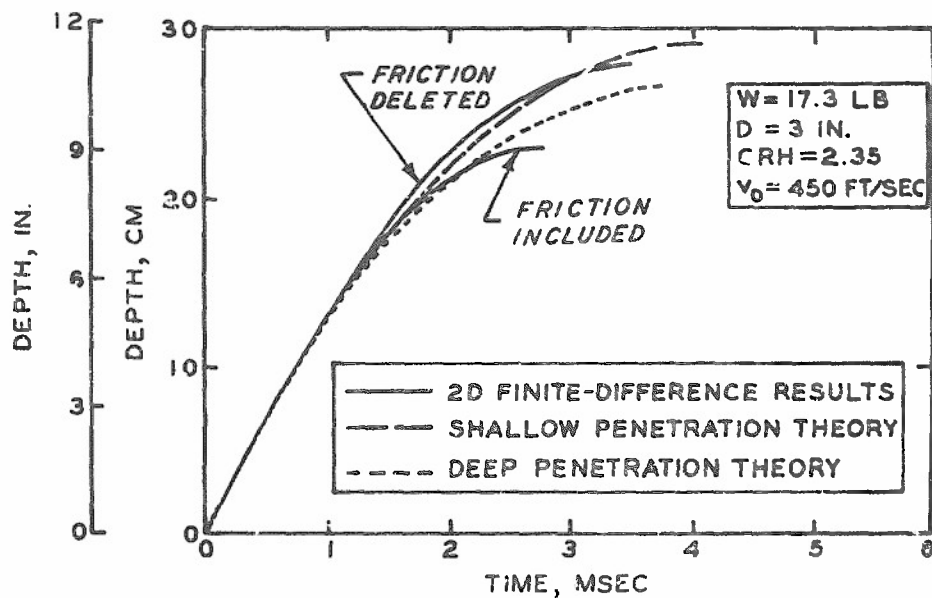in hypothetical frozen soil target

Figure 12. Penetration depth versus time
in hypothetical frozen soil target

49

changed somewhat since its initial formulation by Goodier,[3] it is appropriate to apply the present shallow and deep penetration theories to at least one of the problems which were discussed by Goodier in his original work. Consider the penetration of a homogeneous 2024-T3 aluminum target by spherical steel projectiles. The target properties are

$$\rho_0 = 173 \text{ pcf } (2.77 \text{ gm/cm}^3)$$

$$Y = 5.6 \times 10^4 \text{ psi } (3.86 \text{ kbar})$$

$$E = 10^7 \text{ psi } (689 \text{ kbar})$$

$$E_t = 4.1 \times 10^5 \text{ psi } (28.3 \text{ kbar})$$

and

$$\rho_0 c^2 \cong 10^7 \text{ psi } (689 \text{ kbar})$$

Target compressibility is adequately characterized by Equation 44 for the range of dynamic pressures encountered. Goodier gives his results in nondimensional form, choosing $2q_f/D$ as the nondimensional final penetration depth and $v_0\sqrt{\rho_p/Y}$ as the nondimensional impact velocity. The quantity ρ_p represents the projectile density, where $\rho_p = 491$ pcf (7.82 gm/cm^3) for steel. Consequently, a nondimensional impact velocity $v_0\sqrt{\rho_p/Y} = 1$ is equivalent to $v_0 = 727$ fps (222 m/sec). The predictions of the three penetration theories are compared with experimental results[3,9] in Figure 13. For the experimental results, the range of solid Reynolds numbers at impact is $1 \leqslant R_s \leqslant 20$. The difference between Goodier's results and those of the shallow and deep penetration theories is due primarily to the fact that Goodier uses Meyer's law to characterize target resistance during the projectile embedding process (References 3 and 5). In the present work, Meyer's law is replaced by an equation of motion which is based upon the cavity expansion theory (see Part III, paragraph 22), resulting in reduced penetration depths at the lower velocities.

Shallow Penetration of Concrete

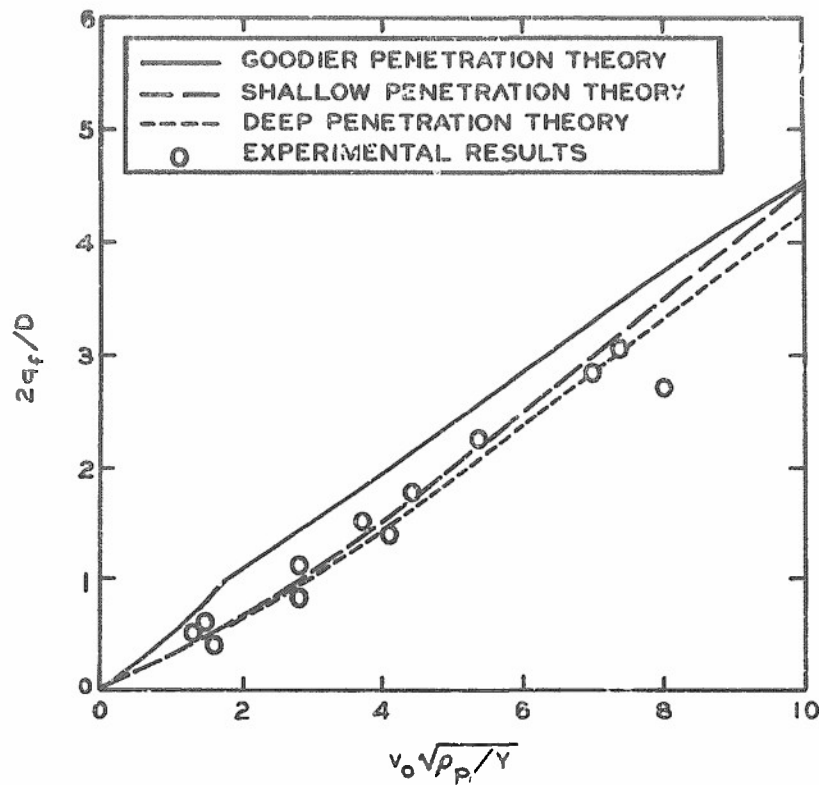45. The penetration of concrete has been the object of extensive

Figure 13. Nondimensional final penetration
depth versus impact velocity for steel spheres
and 2024-T3 aluminum target

experimental study for several decades, and a number of empirical pene-
tration equations have been developed from the resulting data. For
example, a fairly reliable equation for the penetration of reinforced
concrete by various types of projectiles is given by[10]

$$q_f = \frac{222 \; W \; D^{0.215} \left(\dfrac{v_o}{1000}\right)^{1.5}}{A \sqrt{Y}} + \frac{D}{2} \pm 15\% \tag{118}$$

where q_f is specified in inches, W in pounds, D in inches, v_o in
fps, A in square inches, and Y in psi. No range of applicability is
defined for this equation, but sample calculations given in Reference 10
lie in the range 152 m/sec $\leq v_o \leq 762$ m/sec (i.e., 500 fps $\leq v_o \leq 2500$
fps). For comparison with penetration theory predictions, the above
equation will be used to make calculations in the velocity range
100 m/sec $\leq v_o \leq 1000$ m/sec (328 fps $\leq v_o \leq 3280$ fps), corresponding to
$0.7 \leq R_s \leq 70$ at impact. The concrete static properties are[11]

51

$$\rho_0 = 150 \text{ pcf } (2.40 \text{ gm/cm}^3)$$

$$Y = 5000 \text{ psi } (0.345 \text{ kbar})$$

$$E \cong 4.10 \times 10^6 \text{ psi } (283 \text{ kbar})$$

and

$$E_t = 0$$

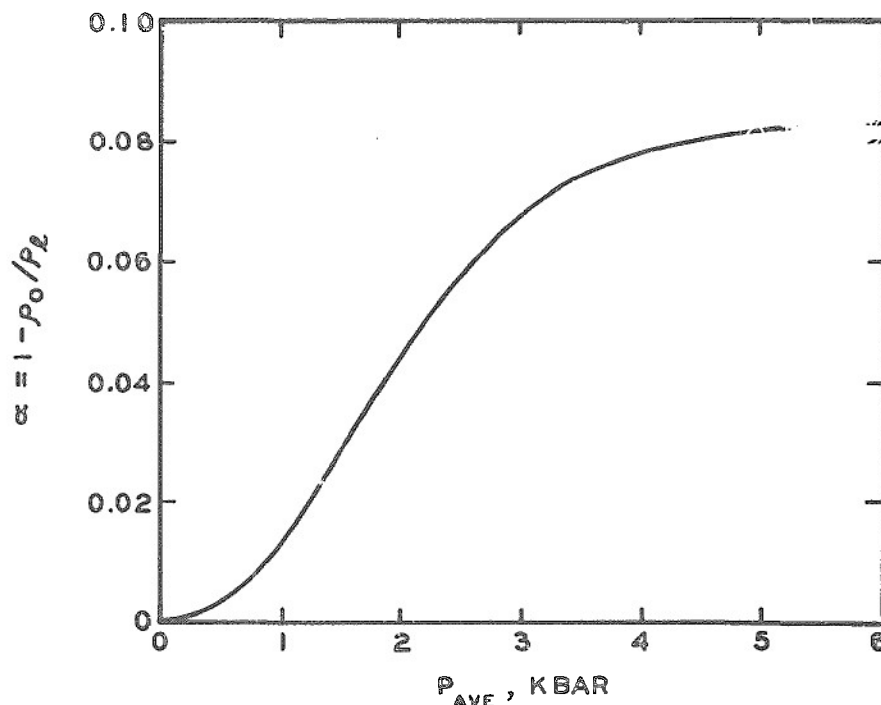The pressure-density relation[12] illustrated in Figure 14 represents

Figure 14. Typical pressure-density relation
for concrete

typical behavior of concrete under pressure. The static value of Y
is used in the theoretical calculations as well as in Equation 118, and
the resulting theoretical predictions of final penetration depth then
correspond to upper-bound values. However, if a maximum dynamic value
of Y (i.e., 40 percent higher than the static value) is chosen, the
theoretical penetration depths are reduced by only about 15 percent.
Since Equation 118 does not account for projectile geometry, two sep-
arate ogive nose shapes are used in the theoretical calculations,
CRH = 1.25 (L/D = 1) and CRH = 9.25 (L/D = 3) . Otherwise, the pro-
jectile characteristics are chosen to be W = 1000 lb (455 kg) and

D = 12 in. (30.5 cm) , which are typical of the projectiles for which Equation 118 was deduced. Results are compared in Figure 15, which shows good agreement between empirical and theoretical predictions.
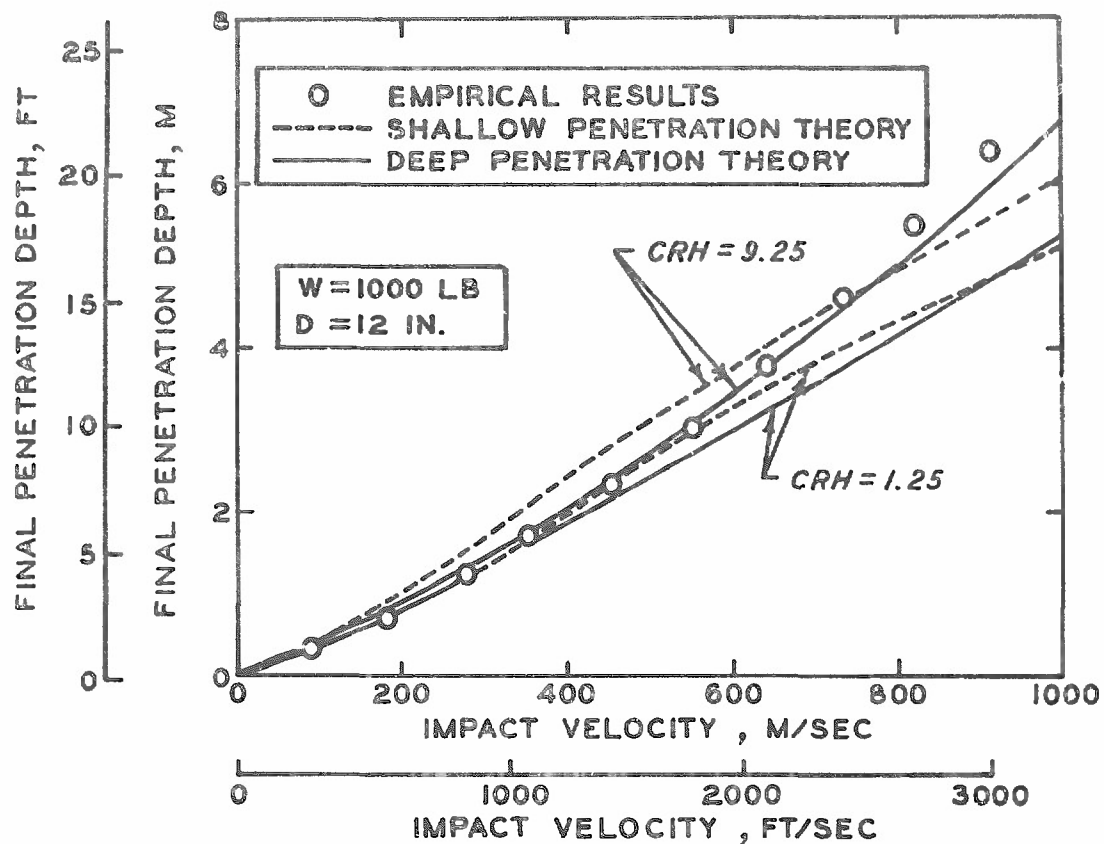

Figure 15. Final penetration depth versus impact velocity for 5000-psi concrete

Perforation of an Aluminum Slab

46. Wilkins[13] has performed 2D finite-difference calculations analyzing the perforation of an aluminum slab by a sharp steel projectile. This sort of problem is of particular interest in the present investigation since it represents an extreme example of penetration in a layered target. The first layer is the slab, which has a finite thickness as well as a finite density, yield strength, and elastic modulus; the second layer is air, which has a negligible density and no resistance at all to shear (i.e., the second layer is a fluid, in which $R_s = \infty$ for all $\dot{q} > 0$). Wilkins makes two separate calculations: (a) in his first calculation, the ultimate strength of 6061-T6 aluminum

53

is used as the target yield strength; and (b) in his second calculation, this yield strength is doubled. The predictions of the shallow and deep penetration theories for layered targets will now be compared with Wilkins' results. The aluminum slab has a thickness of 1 in. (2.54 cm), and the nominal target properties are

$$\rho_0 = 169 \text{ pcf } (2.7 \text{ gm/cm}^3)$$

$$Y = 43,500 \text{ psi } (3 \text{ kbar})$$

$$E \cong 10^7 \text{ psi } (689 \text{ kbar})$$

$$E_t \cong 0$$

and

$$\rho_0 c^2 \cong 10^7 \text{ psi } (689 \text{ kbar})$$

Target compressibility is adequately characterized by Equation 44 for the range of dynamic pressures encountered. The projectile characteristics are

$$W = 0.0183 \text{ lb } (8.32 \text{ gm})$$

$$D = 0.3 \text{ in. } (0.762 \text{ cm})$$

$$L/D = 1 \text{ (conical nose)}$$

and

$$v_o = 2756 \text{ fps } (840 \text{ m/sec})$$

47. Since Wilkins does not give deceleration histories for the projectile, the most stringent comparison of 2D and theoretical results lies in the examination of residual projectile kinetic energy (i.e., the kinetic energy of the projectile after it has passed completely through the slab). Theoretical and 2D predictions of residual kinetic energy are compared in nondimensional form in Figure 16, where v_r is the residual projectile velocity and $v_o\sqrt{\rho_0/Y}$ is chosen as the non-dimensional impact velocity (note that $v_o\sqrt{\rho_0/Y} = \sqrt{R_s}$ at impact). The variation of nondimensional impact velocity is achieved by varying Y instead of v_o, and the predictions of kinetic energy <u>loss</u> exceed Wilkins' values by as much as 75 percent, which may be considered "good"
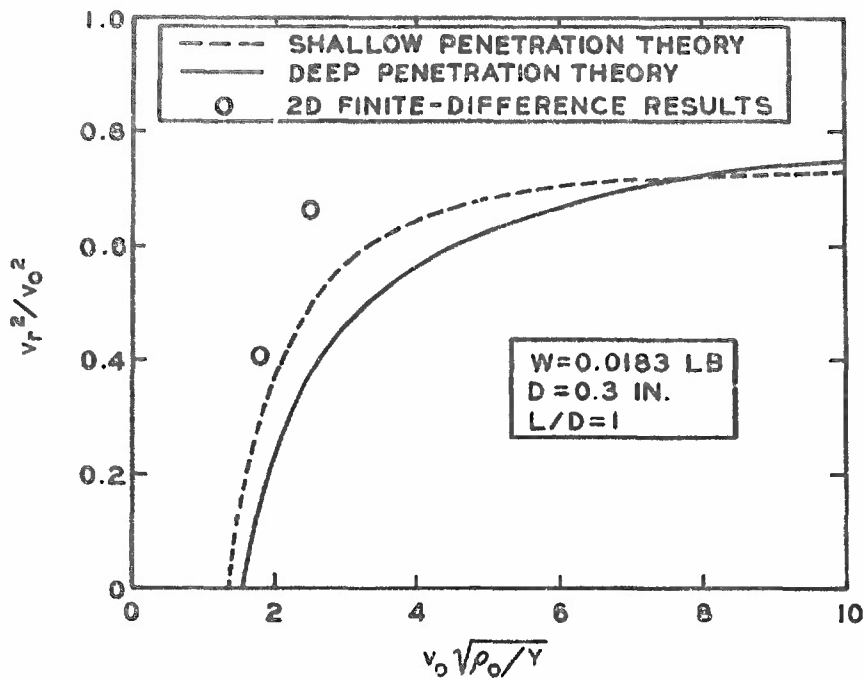
Figure 16. Nondimensional residual kinetic
energy versus impact velocity for conical
nosed steel projectile after perforating
1-in.-thick aluminum slab

or "bad" depending on one's viewpoint. (Wilkins' results for Y = 3 kbar
are in agreement with experiment.[13]) This example indicates to some
extent the accuracy with which the two penetration theories predict
projectile deceleration and energy loss at low to moderate values of
R_s near an interface between two layers which have extremely different
material properties. At low values of R_s , the deep penetration theory
predicts higher energy loss than the shallow penetration theory, but
this trend is reversed as R_s increases.

Deep Penetration of a Multilayer Earth Target

48. In July of 1974, the Defense Nuclear Agency (DNA) sponsored
a series of large-scale projectile penetration tests which were con-
ducted by Sandia Laboratories at the Watching Hill Blast Range near
Ralston, Alberta, Canada.[14] The three test projectiles ranged in weight
from 200 to 400 lb (91 to 182 kg), final penetration depths ranged from
30 to 99 ft (9 to 30 m), and impact velocities ranged from 306 to
619 fps (93 to 189 m/sec). This represents one of the best documented

large-scale earth penetration experiments ever conducted, consisting of eight successful shots into a target which had been previously subjected to an extensive material property investigation. A summary of the test results is given in Table 2, which is taken directly from Reference 14.

49. The shallow and deep penetration theories will now be used to calculate projectile motion in the idealized four-layer target site. Bilinear shear properties and initial densities are tabulated for the target in Table 3 ($E_t = 0$ for all layers). These properties were used in a pretest calculation by Rohani[15] and are obtained from the results of unconfined dynamic tests.[14] The relation between density and pressure[14] is given for each layer in Figure 17. The projectile weights and diameters are 200 lb (91 kg), 280 lb (127 kg), 400 lb (182 kg), and 4.125 in. (10.48 cm), 6 in. (15.24 cm), 6.5 in. (16.51 cm), respectively. The 400-lb projectile has a 9.25 CRH ogive nose shape (L/D = 3); the other two have 6.0 CRH ogive nose shapes (L/D = 2.4). Comparisons of theoretical and experimental final penetration depths are given in Figures 18-20, and a comparison of theoretical and experimental deceleration records for Test No. 6 is shown in Figure 21. These calculations fall in the range of moderate to high solid Reynolds number ($R_s \sim 10^2$), and the shallow penetration theory exhibits an increasing tendency to underpredict final penetration depth at the higher impact velocities (i.e., at the higher values of R_s). On the other hand, the deep penetration theory reproduces the observed final depths with fair accuracy. Examination of the deceleration records in Figure 21 reveals that neither theory duplicates the details of the experimental deceleration curve; however, the deep penetration theory predicts decelerations which are more nearly in agreement with the experimental results.

Very Deep Penetration of a Multilayer Earth Target

50. Some of the deepest earth penetration events on record were observed in tests conducted by Sandia Laboratories at the Tonopah Test Range (TTR) near Tonopah, Nevada. The results of these tests are

Table 2

Watching Hill Test Results

Test No.	Projectile Description Diam in.	Length in.	Weight lb	W/A psi	Depth to Nose Tip ft	Velocity at Impact Printed Circuit Board ft/sec	Image Motion ft/sec	Time to Maximum Penetration msec	Maximum Deceleration* Raw Data g's	450 Hz Filtered g's	200 Hz Filtered g's	Remarks
01	6.0	48	280	9.9	73.2	583	571	>270	(-) 180	(327) --	(360) 175	Instrumented projectile
02	6.5	60	400	12.1	48.3	429	410	≅270	(-) 141	(102) --	(85) 94	Instrumented projectile
03	6.0	48	280	9.9	39.8	409	402	--	--	--	--	
04	6.0	48	280	9.9	65.7	520	512	--	--	--	--	
05	6.5	60	400	12.1	1.1	?	?	--	--	--	--	Bad burn
06	6.5	60	400	12.1	67.9	493	478	>195	(-) 200*	(170) --	(136) 116	Instrumented projectile, test case
07	6.5	60	400	12.1	29.8	306	305	≅180	(-) 147	(87) --	(68) 71	Instrumented projectile, complete time history obtained
08	4.125	60	200	15.0	99.0	--	650	--	--	--	--	
09	4.125	60	200	15.0	86.1	619	611	--	--	--	--	

* Quantities in parentheses were derived from data recorded on a high-frequency early time recording system. The other decelerations tabulated are based on data from a low-frequency on-board digital recorder.

57

Table 3

Material Properties for Watching Hill Test Site

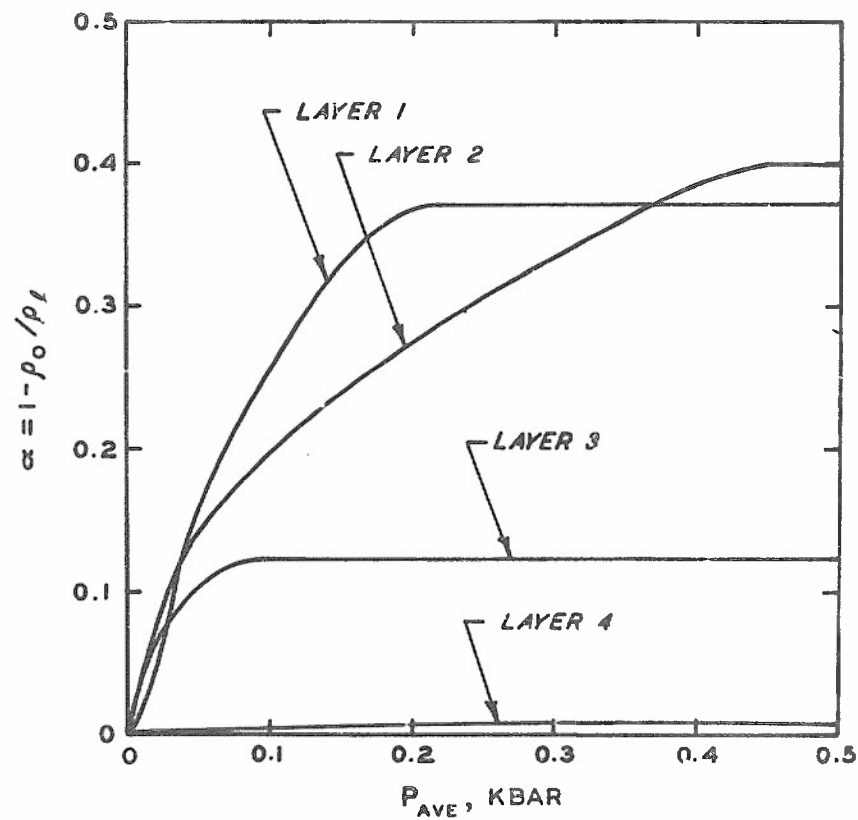| Layer No.	ρ_0 pcf	Y bar	E bar	Depth of Layer Bottom ft
1	93.0	3.10	276.0	8
2	88.6	2.07	138.0	16
3	116.0	2.07	138.0	24
4	123.0	2.07	82.7	∞

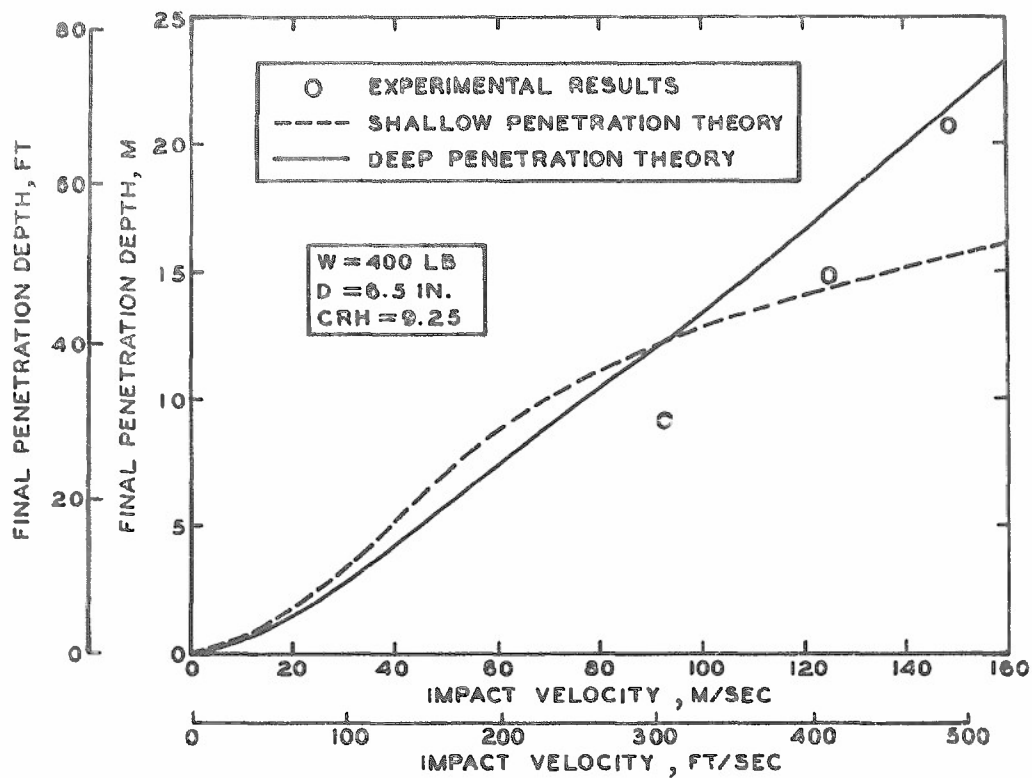Figure 17. Pressure-density relations for Watching Hill test site

Figure 18. Final penetration depth versus impact velocity
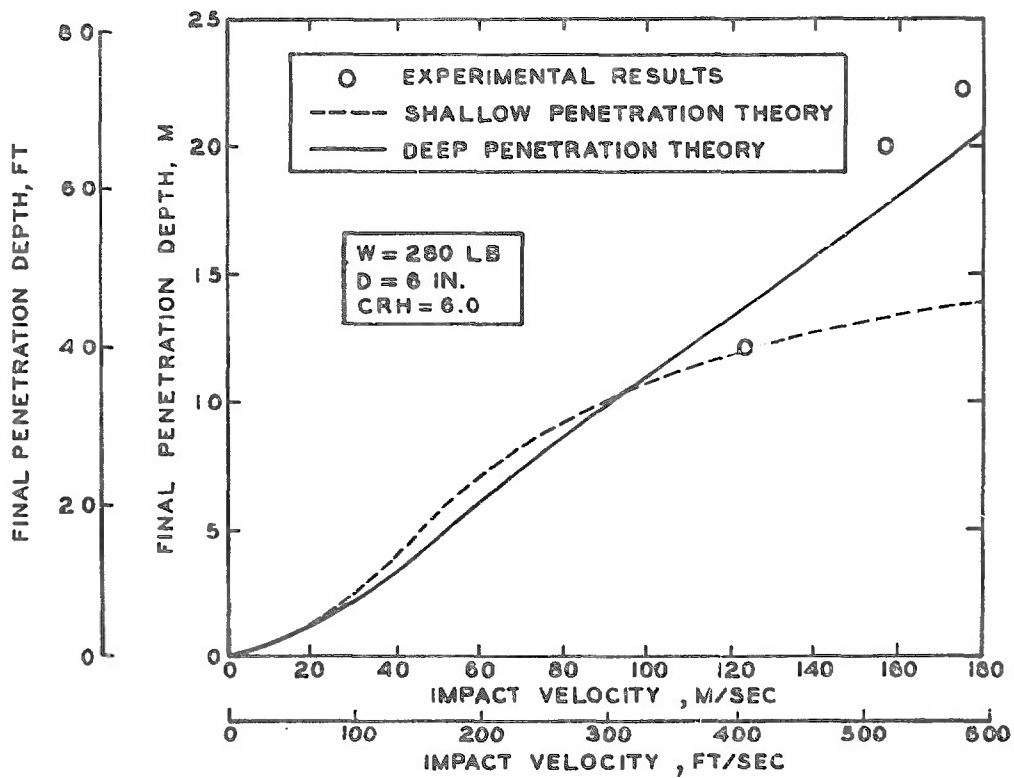for 400-lb Watching Hill test projectile

Figure 19. Final penetration depth versus impact velocity
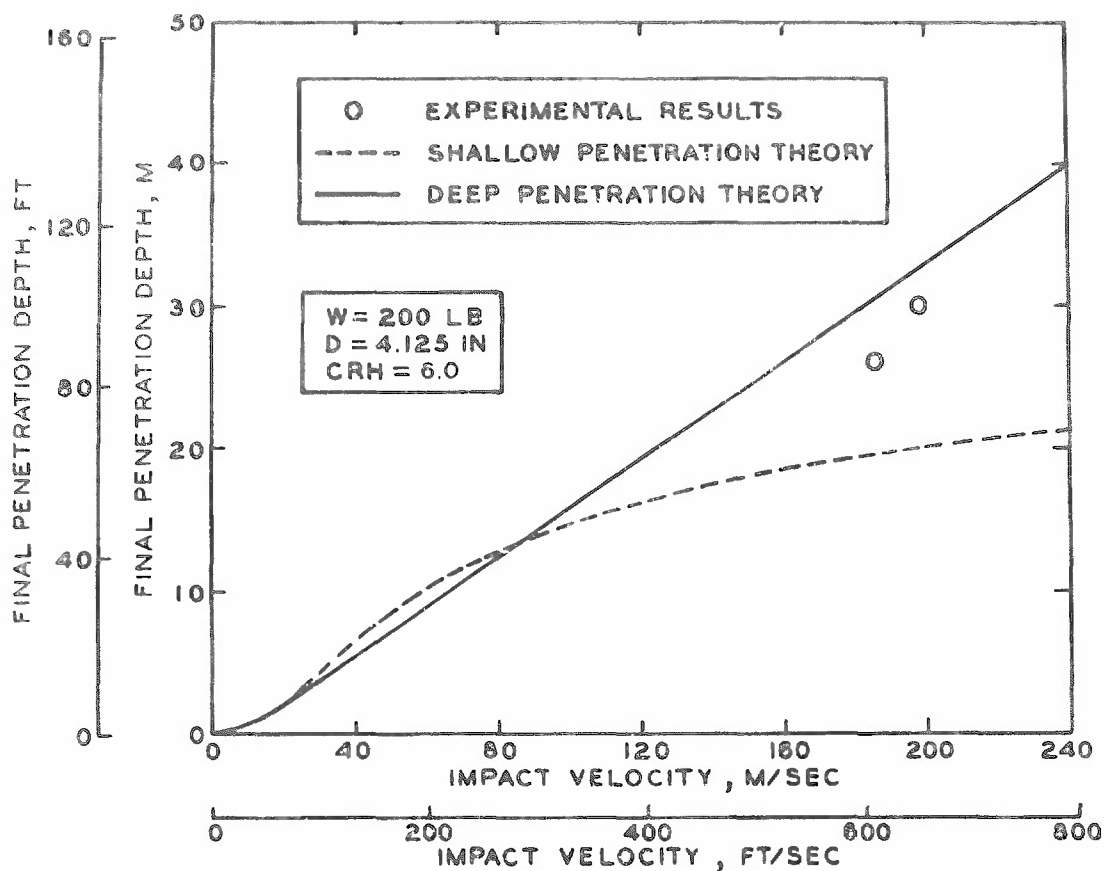for 280-lb Watching Hill test projectile

Figure 20. Final penetration depth versus impact velocity
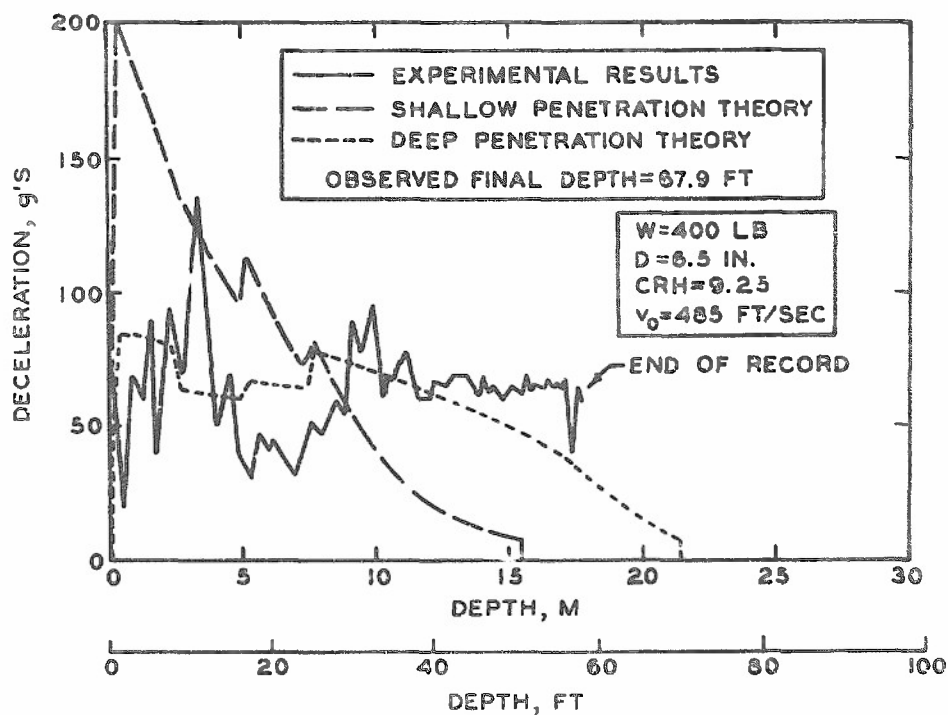for 200-lb Watching Hill test projectile

Figure 21. Projectile deceleration versus depth
for Watching Hill Test No. 6

reported by Patterson[16] for a projectile with the following characteristics:

$$W = 650 \text{ lb } (295 \text{ kg})$$
$$D = 9 \text{ in. } (22.9 \text{ cm})$$
$$CRH = 6.0 \text{ (ogive nose)}$$

Peterson and Hadala[17] have made upper- and lower-bound strength estimates for the Antelope Dry Lake where the tests were conducted. These estimates were made using available unconfined strength data and visual classifications for the Antelope Lake and Main Lake beds along with constitutive property analyses for similar playa deposits at TTR and at the Nevada Test Site. The estimated strengths are listed for the idealized four-layer target in Table 4.

Table 4

Material Properties for TTR Antelope Dry Lake Site

Layer No.	ρ_0 pcf	Lower-Bound Y bar	Upper-Bound Y bar	Depth of Layer Bottom ft
1	103	0.689	3.448	25
2	99	0.001	3.448	37
3	111	5.172	10.345	109
4	103	3.448	10.345	∞

For the upper-bound strengths, $E \approx 150 \text{ Y}$; and for the lower-bound strengths, $E \approx 75 \text{ Y}$. The target is assumed to be incompressible.

51. Experimental and theoretical results for final penetration depth are compared in Figures 22 and 23, with the shaded area representing the range of predicted depths resulting from the estimated bounds on the target properties. The difference in the predictions of the two penetration theories is dramatic: the shallow penetration
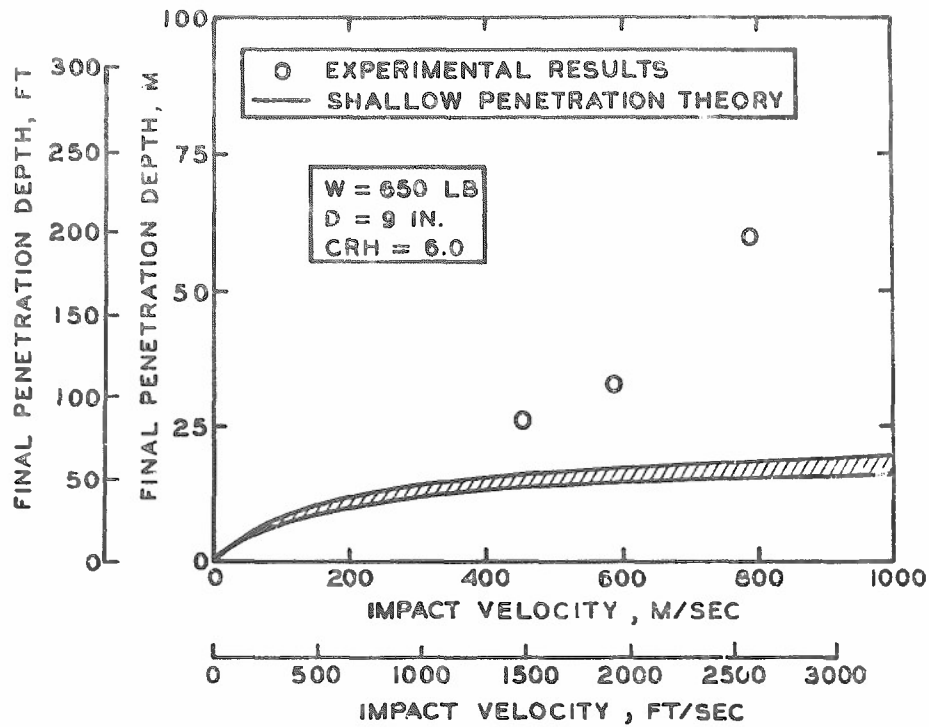
61

Figure 22. Range of final penetration depth versus impact velocity for TTR Antelope Dry Lake, as predicted by the shallow penetration theory
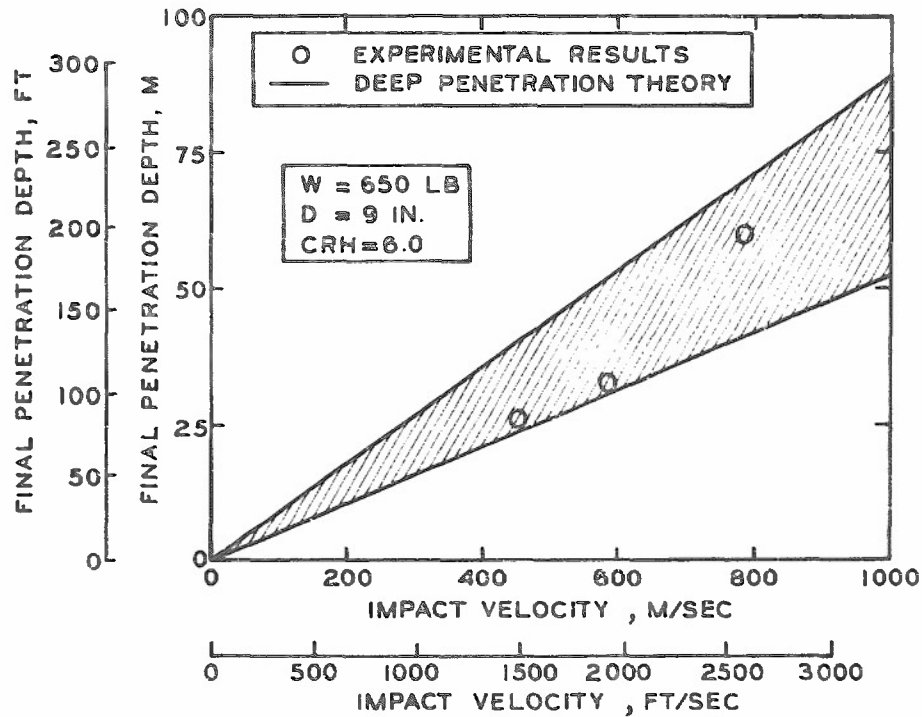

Figure 23. Range of final penetration depth versus impact velocity for TTR Antelope Dry Lake, as predicted by the deep penetration theory

theory exhibits a growing tendency to underpredict final depth with increasing impact velocity, while the deep penetration theory predicts an approximately linear relation between final depth and impact velocity which is in rough agreement with the experimental results. Figure 23 also serves to illustrate the prediction spread which is to be expected when target property estimates are made without the benefit of a detailed investigation of the target site itself. In these calculations, the solid Reynolds number at a velocity of 2500 ft/sec is on the order of $R_s \sim 10^3$. No experimental deceleration records are available.

PART V: CONCLUSIONS AND RECOMMENDATIONS

52. As a result of efforts made under the present research program, the projectile penetration theory originally formulated by Goodier[3] has been extended so that the theory is now applicable for deep penetration as well as for shallow penetration in both homogeneous and layered cohesive targets. The initial formulation of the theory was based on an ad hoc analogy with the dynamic expansion of a spherical cavity in an infinite medium. The final step in the theoretical development was directly empirical in that a single function $\psi(R_s)$ had to be chosen which relates dynamic penetration resistance to the solid Reynolds number as well as to the projectile geometry. This was accomplished by means of a trial and error comparison of experimental and theoretical results, but it is emphasized that the expression for $\psi(R_s)$ which was chosen (Equation 84) is the same for all targets and projectiles. The deep penetration theory now represents a self-contained tool for making penetration predictions and requires only the projectile characteristics and the target constitutive properties as input.

53. The deep penetration theory is most applicable for cohesive targets, such as metal, rock, and concrete. On the other hand, it is least applicable for granular targets, such as sand, which exhibit a strong dependence between shear strength and confining pressure.

54. The comparisons of theoretical and experimental results for cohesive targets in Part IV suggest reliability at solid Reynolds numbers as high as $R_s \sim 10^3$, at least for nose shapes with $L/D \geq 1$. For $L/D < 1$, the range of reliability probably decreases with decreasing L/D. When $L/D \geq 1$, the theory results in an approximately linear relation between final penetration depth and impact velocity, which is consistent with experimental observation. The theory also predicts an approximately linear relation between final depth and projectile frontal loading W/A, as well as a nonlinear relation between final depth and projectile nose length.

55. In those cases where it is applicable, the deep penetration

theory can generally be expected to predict peak deceleration within about a factor of two and final penetration depth within about 20 percent when the target density and unconfined strength are known with reasonable accuracy. Other quantities, such as total duration of the penetration event, will probably be accurate within about a factor of two. Error in prediction will, of course, increase as uncertainty in target properties increases.

56. Future efforts should be directed toward further comparison of theoretical and experimental results and toward the development of a penetration theory for materials which are governed by the Mohr-Coulomb failure condition (shear strength proportional to confining pressure). The Mohr-Coulomb condition is more generally applicable to soils than is the Von Mises condition which is used in the present theory.

REFERENCES

1. Bishop, R. F., Hill, R., and Mott, N. F., "The Theory of Indentation and Hardness Tests," Proceedings, Physical Society of London, Vol 57, 1945, pp 147-159.

2. Hopkins, H. G., "Dynamic Expansion of Spherical Cavities in Metals," Progress in Solid Mechanics, R. Hill and I. N. Sneddon, ed., Vol 1, Pergamon Press, Oxford, England, 1960, pp 84-164.

3. Goodier, J. N., "On the Mechanics of Indentation and Cratering in Solid Targets of Strain-Hardening Metal by Impact of Hard and Soft Spheres," Proceedings, Seventh Symposium on Hypervelocity Impact, Vol III, 1965, pp 215-259.

4. Hanagud, S. and Ross, B., "Large Deformation, Deep Penetration Theory for a Compressible Strain-Hardening Target Material," AIAA Journal, Vol 9, No. 5, May 1971, pp 905-911.

5. Bernard, R. S. and Hanagud, S. V., "Development of a Projectile Penetration Theory; Penetration Theory for Shallow to Moderate Depths," Technical Report S-75-9, Report 1, Jun 1975, U. S. Army Engineer Waterways Experiment Station, CE, Vicksburg, Miss.

6. Thigpen, L., "Projectile Penetration of Elastic-Plastic Earth Media," Journal, Geotechnical Engineering Division, American Society of Civil Engineers, Vol 100, No. GT3, Mar 1974, pp 279-294.

7. Patterson, W. J., "Penetration of In Situ Rock by Air Deliverable Penetrators," Proceedings, Conference on Rapid Penetration of Terrestrial Materials, Texas A&M University, College Station, Tex., Feb 1972, pp 453-473.

8. Ito, Y. M. et al., "Analysis of Dynamic Stresses Within a Terminal Delivery Vehicle During Penetration of a Hard Earth Target," Contract Report S-75-1, Feb 1975, U. S. Army Engineer Waterways Experiment Station, CE, Vicksburg, Miss.; prepared by California Research and Technology, Inc., under Contract No. DACA39-74-C-0015.

9. Herrman, W. and Jones, A. H., "Survey of Hypervelocity Impact Information," Report No. 99-1, Sep 1961, Aeroelastic and Structures Research Laboratory, Massachusetts Institute of Technology, Cambridge, Mass.

10. Headquarters, Department of the Army, "Protective Design: Fundamentals of Protective Design (Non-Nuclear)," Technical Manual TM 5-855-1, 19 Jul 1965, Washington, D. C.

11. Lin, T. Y., Design of Prestressed Concrete Structures, 2d ed., Wiley, New York, 1963, pp 37-38.

12. Gregson, V. G., Jr., "A Shock Wave Study of Fondu-Fyre WA-1 and a Concrete," Report No. MSL-70-30 (DNA 2797F), 1972, Materials and Structures Laboratory, General Motors Technical Center, Warren, Mich.

13. Wilkins, M. L., "Penetration Mechanics," Preprint No. UCRL-72111 (prepared for and submitted to Yale Scientific Magazine), Nov 1969, Lawrence Radiation Laboratory, University of California, Livermore, Calif.

14. Hadala, P. F., "Evaluation of Empirical and Analytical Procedures Used for Predicting the Rigid Body Motion of an Earth Penetrator," Miscellaneous Paper S-75-15, Jun 1975, U. S. Army Engineer Waterways Experiment Station, CE, Vicksburg, Miss.

15. Rohani, B., "Pretest Penetration Calculations for DNA Earth Penetrator Experiments at DRES, Canada" (unpublished report), Jun 1974, U. S. Army Engineer Waterways Experiment Station, CE, Vicksburg, Miss.

16. Patterson, W. J., "Terradynamic Results and Structural Performance of a 650-Pound Penetrator Impacting at 2570 Feet per Second," Report No. SC-DR-69-782, Dec 1969, Sandia Laboratories, Albuquerque, N. Mex.

17. Peterson, R. W. and Hadala, P. F., "Shear Strength Properties for the Antelope Lake, Tonopah Test Range, Nevada," Memorandum for Record, 13 Jan 1976, Soil Dynamics Division, U. S. Army Engineer Waterways Experiment Station, CE, Vicksburg, Miss.

$a, \dot{a}, \ddot{a}$ Radial position, velocity, and acceleration, respectively, of spherical cavity wall†

a_I Projectile radius at layer interface location

a_o Maximum projectile radius = D/2 (Figures 3 and 4)

a_s Projectile radius at target surface

A Maximum projectile cross-section area = $\pi a_o^2 = \pi D^2/4$

b Radial position of spherical plastic front (Figure 1)

b_o Initial radial position of particle located at position b

B_1, B_2 Cavity expansion inertial coefficients (Equations 40 and 41)††

C Dilatational wave speed

CRH Ogive caliber radius (Equation 67)

D Maximum projectile diameter = $2a_o$ (Figures 3 and 4)

E Modulus of elasticity in compression

E_t Strain-hardening modulus in compression

f_e, f_ℓ Functions of integration (Equations 4, 9, and 11)

f_n Projectile nose shape factor (Equations 62, 63, 65, 72, and 78)

f_{n*} Effective nose shape factor near a layer interface (Equation 94)

F_z Net axial resisting force exerted on projectile by target

g Gravitational acceleration = 32.2 ft/sec^2 (9.8 m/sec^2)

h Radial position of interface between two concentric layers (Figure 1)

h_o Initial radial position of interface between two concentric layers

H Distance from base of projectile nose to layer interface location (Figure 5)

L Projectile nose length (Figures 3 and 4)

m Summation index

M Projectile mass

---

†   A dot above any quantity denotes differentiation with respect to time.

††   With the exception of B_1 and B_2, the subscripts 1 and 2 denote first and second layer quantities, respectively.

p	Compressive normal stress at cavity surface (Equations 7 and 30) and at projectile frontal surface (Equation 48)
p_I	Dynamic pressure at cavity surface (Equation 38) and at projectile frontal surface (Equation 49)
p_s	Compressive normal stress at cavity surface due to material behavior in shear (Equation 39)
P_{ave}	Volume-averaged dynamic pressure in plastic region (Equations 42 and 107)
$q, \dot{q}, \ddot{q}$	Projectile penetration depth, velocity, and acceleration, respectively
q_f	Final penetration depth
r	Eulerian radial coordinate
r_o	Initial radial position of particle located at position r
R	Shown in Figure 4
R_s	Solid Reynolds number (Equation 68)
S	Effective distance from base of projectile nose to plastic front (Figure 5)
t	Time
v	Outward radial particle velocity
v_n, v_t	Components of v_p, respectively, normal and tangent to projectile frontal surface (Figure 3)
v_o	Projectile impact velocity
v_p	Target particle velocity adjacent to projectile frontal surface (Figure 3)
v_r	Residual projectile velocity
W	Projectile weight
x	Nondimensional cone position (Equation 52)
x_e	Equivalent nondimensional cone position for ogive (Equation 55)
Y	Yield strength in compression
z	Axial distance measured aft of projectile nose tip (Figures 3 and 4)
α	Material compaction coefficient (Equation 12)
β, δ	Nondimensional material parameters (Equations 17 and 24)
$\Delta\sigma_b$	Discontinuity in σ_r at $r = b(t)$
ε	Ogive parameter (Equation 67)
ε_ℓ	Locking strain (Equation 1)

$\varepsilon_r, \varepsilon_\theta$ Normal strains in radial and circumferential directions, respectively

η Shown in Figure 4

ξ Nondimensional depth (Equation 115)

π 3.1416

ρ Material density

ρ_ℓ Locked plastic density

ρ_p Projectile density

ρ_0 Initial density

$\sigma_b^{(+)}$ Limiting value of σ_r as $r \to b$ in the elastic region

$\sigma_b^{(-)}$ Limiting value of σ_r as $r \to b$ in the locked plastic region

σ_r, σ_θ Normal stresses in radial and circumferential directions, respectively

ϕ Cone half-angle (Figure 3)

ϕ_e Equivalent cone half-angle for ogive

ψ Function relating v_t and R_s (Equations 69 and 84)

Bernard, Robert S
    Development of a projectile penetration theory;
  Report 2: Deep penetration theory for homogeneous and
  layered targets, by Robert S. Bernard. Vicksburg, U. S.
  Army Engineer Waterways Experiment Station, 1976.
    1 v. (various pagings) illus. 27 cm. (U. S.
  Waterways Experiment Station. Technical report S-75-9,
  Report 2)
    Prepared for Office, Chief of Engineers, U. S. Army,
  Washington, D. C., under Project 4A161102B52E, Task 04,
  Work Unit 13.
    Includes bibliography.

    1. Projectile penetration.   I. U. S. Army. Corps
  of Engineers.   (Series: U. S. Waterways Experiment
  Station, Vicksburg, Miss. Technical report S-75-9,
  Report 2)
  TA7.W34 no.S-75-9 Report 2